

ALMA measures rapidly depleted molecular gas reservoirs in massive quiescent galaxies at  $z \sim 1.5$

CHRISTINA C. WILLIAMS,<sup>1,\*</sup> JUSTIN S. SPILKER,<sup>2,†</sup> KATHERINE E. WHITAKER,<sup>3,4</sup> ROMEEL DAVÉ,<sup>5</sup> CHARITY WOODRUM,<sup>1</sup>  
GABRIEL BRAMMER,<sup>6,4</sup> RACHEL BEZANSON,<sup>7</sup> DESIKA NARAYANAN,<sup>8,4</sup> AND BENJAMIN WEINER<sup>1</sup>

<sup>1</sup>*Steward Observatory, University of Arizona, 933 North Cherry Avenue, Tucson, AZ 85721, USA*

<sup>2</sup>*Department of Astronomy, University of Texas at Austin, 2515 Speedway, Stop C1400, Austin, TX 78712, USA*

<sup>3</sup>*Department of Astronomy, University of Massachusetts, Amherst, 710 N. Pleasant Street, Amherst, MA 01003, USA*

<sup>4</sup>*Cosmic Dawn Center (DAWN)*

<sup>5</sup>*Institute for Astronomy, Royal Observatory, Edinburgh EH9 3HJ, United Kingdom*

<sup>6</sup>*Niels Bohr Institute, University of Copenhagen, Lyngbyvej 2, DK-2100 Copenhagen, Denmark*

<sup>7</sup>*Department of Physics and Astronomy and PITT PACC, University of Pittsburgh, Pittsburgh, PA, 15260, USA*

<sup>8</sup>*Department of Astronomy, University of Florida, 211 Bryant Space Science Center, Gainesville, FL 32611, USA*

## ABSTRACT

We present ALMA CO(2–1) spectroscopy of 6 massive ( $\log_{10} M_*/M_\odot > 11.3$ ) quiescent galaxies at  $z \sim 1.5$ . These data represent the largest sample using CO emission to trace molecular gas in quiescent galaxies above  $z > 1$ , achieving an average  $3\sigma$  sensitivity of  $M_{\text{H}_2} \sim 10^{10} M_\odot$ . We detect one galaxy at  $4\sigma$  significance and place upper limits on the molecular gas reservoirs of the other 5, finding molecular gas mass fractions  $M_{\text{H}_2}/M_* = f_{\text{H}_2} < 2 - 6\%$  ( $3\sigma$  upper limits). This is 1-2 orders of magnitude lower than coeval star-forming galaxies at similar stellar mass, and comparable to galaxies at  $z = 0$  with similarly low sSFR. This indicates that their molecular gas reservoirs were rapidly and efficiently used up or destroyed, and that gas fractions are uniformly low ( $< 6\%$ ) despite the structural diversity of our sample. The implied rapid depletion time of molecular gas ( $t_{\text{dep}} < 0.6$  Gyr) disagrees with extrapolations of empirical scaling relations to low sSFR. We find that our low gas fractions are instead in agreement with predictions from both the recent SIMBA cosmological simulation, and from analytical “bathtub” models for gas accretion onto galaxies in massive dark matter halos ( $\log_{10} M_{\text{halo}}/M_\odot \sim 14$  at  $z = 0$ ). Such high mass halos reach a critical mass of  $\log_{10} M_{\text{halo}}/M_\odot > 12$  by  $z \sim 4$  that halt the accretion of baryons early in the Universe. Our data is consistent with a simple picture where galaxies truncate accretion and then consume the existing gas at or faster than typical main sequence rates. Alternatively, we cannot rule out that these galaxies reside in lower mass halos, and low gas fractions may instead reflect either stronger feedback, or more efficient gas consumption.

## 1. INTRODUCTION

A challenge of modern galaxy evolution is to understand the formation of massive and quiescent galaxies. Stellar archaeology indicates that massive galaxies ( $\log_{10} M_*/M_\odot > 11$ ) form their stars in a rapid burst in the first 1-3 billion years of the universe ( $z > 2$ ) (e.g. Thomas et al. 2010; McDermid et al. 2015). After this rapid growth phase, their star formation halted (quenched) through unknown processes, and most remain dormant, without significant star formation for  $> 10$  billion years (e.g. Renzini 2006; Citro et al. 2016).

The observed rapid growth and early death in quenched galaxies are longstanding problems in our theoretical understanding of galaxy formation. This is

particularly true for high mass galaxies at high redshifts, which have caused the largest tension with simulations in terms of reproducing numbers (e.g. Santini et al. 2012; Cecchi et al. 2019) and halting and preventing further star formation (e.g. Croton et al. 2006; Naab & Ostriker 2017; Forrest et al. 2020). Recent improvements to the physical models that are implemented in cosmological simulations are well matched to the observed properties of massive quiescent galaxies at least from  $z < 2.5$ , the growth of their black holes, and the maintenance of quiescence across cosmic time (e.g. Schaye et al. 2015; Feldmann et al. 2017; Nelson et al. 2018; Pillepich et al. 2018). However, even with recent advances, simulations generally require some form of poorly understood, yet extreme feedback to truncate star formation and reproduce the properties of observed massive galaxies across cosmic time (for a review see Somerville & Davé 2015).

\* NSF Fellow

† NHFP Hubble Fellow

A key unknown is the evolution of the cold gas reservoirs, the fuel for star formation, in massive galaxies as they transition from star forming to quiescent. While the majority of massive galaxies quench around cosmic noon ( $1 < z < 3$ ; Whitaker et al. 2011; Muzzin et al. 2013b; Tomczak et al. 2014; Davidzon et al. 2017), surveys characterizing the molecular gas reservoirs using rotational transitions of CO generally find that cold gas is abundant in massive star forming galaxies during this era. The continuity of the star forming sequence implies high accretion rates from the intergalactic medium (for reviews, see Tacconi et al. 2020; Hodge & da Cunha 2020).

To quench, galaxies must break this equilibrium. To sufficiently deplete, expel, or heat the abundant gas supply in massive galaxies, theoretical quenching models favor strong feedback from supermassive black holes (Choi et al. 2017; Weinberger et al. 2017, 2018) or extreme star formation (Hopkins et al. 2010; Grudić et al. 2019). These may be driven by efficient and rapid growth (Wellons et al. 2015; Williams et al. 2014, 2015), mergers (Di Matteo et al. 2005; Hopkins et al. 2006) or disk-instabilities (Dekel & Burkert 2014; Zolotov et al. 2015). Additional theories exist to stabilize existing cold gas from collapse, e.g. through the growth of a stellar bulge (Martig et al. 2009), thereby decreasing the star formation efficiency to quench. However, this likely requires that accretion be halted (through shock-heating at the virial radius for massive dark matter halos with  $\log_{10} M_{\text{halo}}/M_{\odot} > 12$ ; e.g. Birnboim & Dekel 2003; Kereš et al. 2005; Dekel & Birnboim 2006). To first order, these different mechanisms (destruction by feedback, consumption, or stabilization) yield different predictions for the rate at which cold gas disappears from galaxies relative to ceasing star formation.

The evolution of molecular gas reservoirs in quiescent galaxies is therefore an important constraint on the possible mechanisms halting star formation. Several surveys have characterized molecular gas in massive quiescent galaxies using CO at  $z \sim 0$  (Young et al. 2011; Saintonge et al. 2011, 2012, 2017; Davis et al. 2016), generally finding that galaxies maintain low gas fractions ( $< 0.1$ -1%) after  $\gtrsim 10$  Gyr of quiescence. However, the peak epoch of the transition to quiescence for massive galaxies is at  $z \sim 2$ , where few observations have been made to date.

Characterizing the distribution of molecular gas reservoirs in quenched galaxies would be a major step forward in understanding the pathways massive galaxies take to quiescence. With this work, we conduct the first survey targeting molecular gas traced by CO(2–1) in a sample of quiescent galaxies above  $z > 1$ . These build on

samples studied at  $z \sim 0$  (Rowlands et al. 2015; French et al. 2015; Alatalo et al. 2016), at intermediate redshifts (Spilker et al. 2018; Suess et al. 2017), and at  $z > 1$ , single galaxies (Sargent et al. 2015; Bezanson et al. 2019), and average properties through stacking dust emission (Gobat et al. 2018). From these studies emerges a wide diversity of molecular gas properties in quenched and quenching galaxies. Key informative constraints on the molecular gas reservoirs include 1) their variation with properties related to quiescence, such as compact stellar density (e.g. Whitaker et al. 2017; Lee et al. 2018), in light of recent reports that age and quenching timescale varies with size and stellar density (Williams et al. 2017; Wu et al. 2018; Belli et al. 2019) and 2) the amount of gas leftover relative to the time galaxies stopped forming stars, tracing the timescale for consumption.

In this paper, we present a new survey with the Atacama Large Millimeter/submillimeter Array (ALMA) targeting the CO(2–1) emission in quiescent galaxies at  $z > 1$ . In Section 2 we present our sample, their stellar population properties, and our ALMA observations of the CO(2–1) emission line. In Section 3, we present our ALMA measurements in the context of other molecular gas surveys, and in Section 4, we discuss our results in the context of theoretical ideas about the formation of quiescent galaxies. We assume a  $\Lambda$ CDM cosmology with  $H_0 = 70 \text{ km s}^{-1} \text{ Mpc}^{-1}$ ,  $\Omega_M = 0.3$ ,  $\Omega_\Lambda = 0.7$ , and a Chabrier (2003) initial mass function (IMF).

## 2. SAMPLE AND DATA

We select ALMA targets from the literature of spectroscopically confirmed quiescent galaxies at redshifts  $1 < z < 1.74$ , where the CO(2–1) molecular transition is observable in ALMA Band 3, and also have state-of-the-art ancillary data (deep rest-frame UV to mid-IR coverage, including high-resolution *Hubble Space Telescope* (HST) WFC3 imaging). We identified the most massive of those published ( $\log_{10} M_*/M_{\odot} > 11.3$ ) that have quiescent stellar populations based on both their rest frame optical spectroscopy, UV-VJ rest-frame colors (Figure 1) and UV+IR star formation rates. Our final sample includes five galaxies in the COSMOS field, which are all confirmed to be quiescent on the basis of deep Balmer absorption features, strong Dn4000, and a lack of strong emission lines, using deep spectroscopy from Keck/LRIS (Bezanson et al. 2013; van de Sande et al. 2013; Belli et al. 2014, 2015) and Subaru/MOIRCS (Onodera et al. 2012). In this study, we combine these five targets with one galaxy from our pilot observation published in Bezanson et al. (2019).

### 2.1. Optical and infrared data

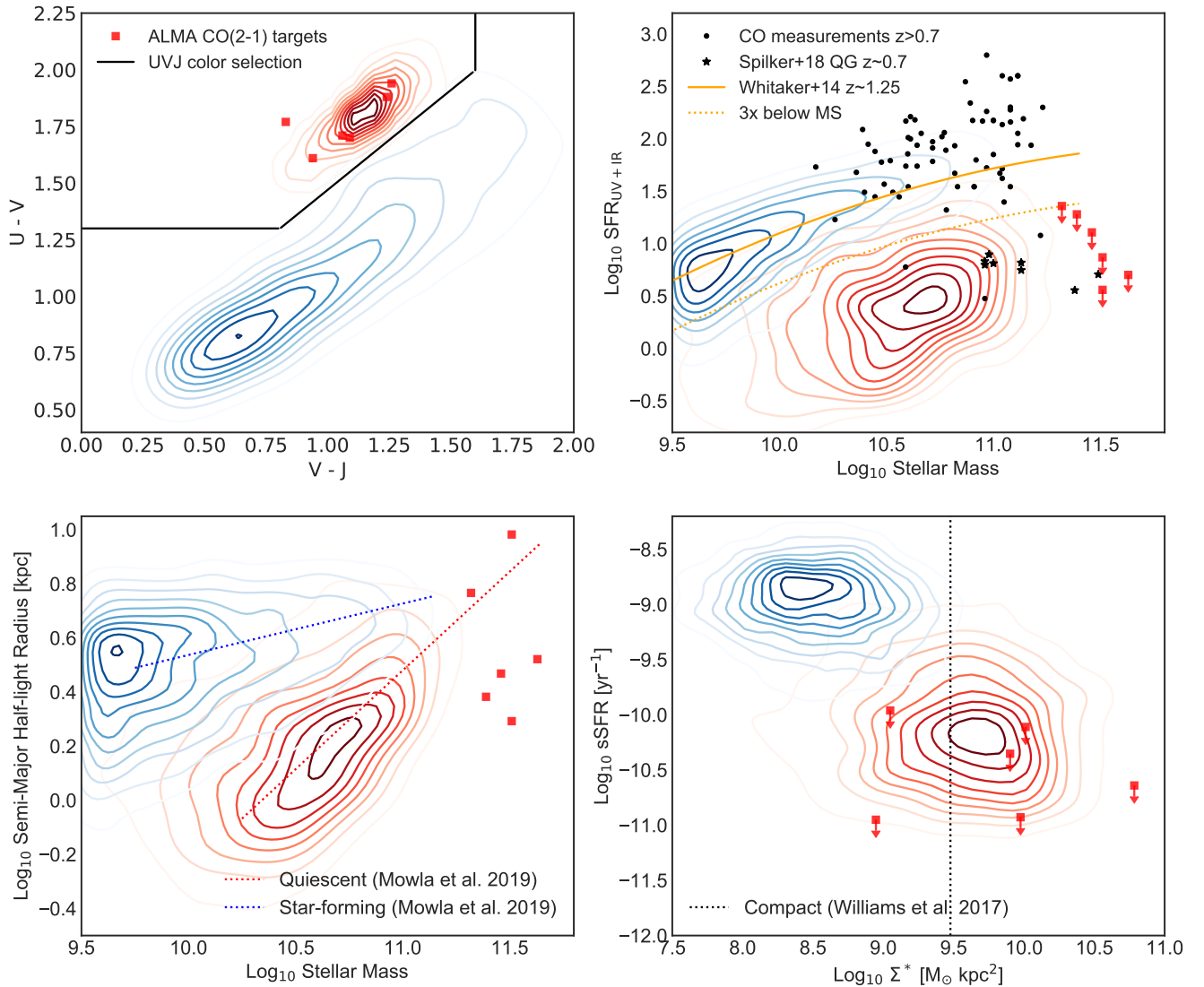


**Figure 1.** Our ALMA targets (red squares) compared to star-forming and quiescent galaxies from 3DHST with  $\log_{10} M_*/M_\odot > 9.5$  at  $1 < z < 1.5$  (blue/red contours Skelton et al. 2014). Top Left:  $U-V$  vs  $V-J$  rest-frame colors and quiescent galaxy selection (black). Top Right: Star formation rate vs stellar mass. Our sample are more than  $3\times$  below the main sequence at  $1 < z < 1.5$  (Whitaker et al. 2014). Black points show CO observations at  $z > 0.7$  for star forming galaxies (see Section 3). Bottom Left: Size vs mass distributions and mean relations at  $z \sim 1.25$  (Mowla et al. 2019). Bottom Right:  $\text{sSFR}$  vs stellar surface density,  $\Sigma_* = M_*/2\pi R_e^2$ . Stellar density higher than the dotted line indicates quiescent galaxies that are compact as defined in (Cassata et al. 2013; Williams et al. 2017). Bottom panels demonstrate that our ALMA sample spans the full range of quiescent galaxy sizes and densities at this redshift.

The five galaxies confirmed with Keck were originally selected for spectroscopy from the NEWFIRM Medium Band Survey (NMBS; Whitaker et al. 2011). NMBS includes multi-wavelength photometry from the UV to  $24 \mu\text{m}$ , and in particular, medium-band near-IR filters that sample the Balmer/4000 Å break at our target redshifts. The Subaru target from the sample of Onodera et al. (2012) was selected from the BzK color-selected catalog published in McCracken et al. (2010).

To identify our target galaxies, we used the stellar masses measured from the photometric spectral energy distribution (SED) as published in the original studies. These works fit the photometry using FAST (Kriek et al. 2009) to estimate stellar masses assuming Bruzual & Charlot (2003) stellar population models with exponentially declining star formation history (SFH), a Chabrier (2003) IMF and Calzetti et al. (2000) dust attenuation. Where relevant, we convert literature measurements to

Chabrier IMF for comparison to our measurements. Not all targets had stellar ages measured in the literature (based on the UV to IR photometry), but where available they indicate old stellar ages (1-1.5 Gyr), with the exception of our pilot galaxy 21434, whose published stellar age is 800 Myr (Bezanson et al. 2019). The pilot galaxy’s rest-frame colors are also the closest to the bluer post-starburst region of the UVJ-quiescent diagram (Whitaker et al. 2012; Belli et al. 2019).

For results presented herein, we re-fit the UV to near-IR photometry uniformly using the SED-fitting code PROSPECTOR (Johnson et al. 2019), which uses the Flexible Stellar Populations Synthesis (FSPS) code (Conroy et al. 2009; Conroy & Gunn 2010). We fit using the PROSPECTOR- $\alpha$  model framework (Leja et al. 2017) which includes a non-parametric SFH that has been shown to be more realistic and physically representative of massive galaxies (Leja et al. 2019a). For the purpose of fitting the stellar population properties probed by the UV to near-IR photometry, we augment the PROSPECTOR- $\alpha$  model by removing emission due to active galactic nuclei (AGN; which contribute primarily at mid-IR wavelengths) and the dust emission. Refitting the galaxies uniformly in this way also enables us to measure the mass-weighted age, which is more directly comparable to the cosmological simulations we present in Section 4.

We use the NMBS photometric catalog that includes medium band near-infrared photometry for all galaxies, with the exception of one (ID 307881) which lies outside the NMBS footprint. For this galaxy we use the UltraVISTA catalog with broad-band photometry in the near-infrared (Muzzin et al. 2013a). We present the stellar population properties measured with PROSPECTOR using the modified PROSPECTOR- $\alpha$  model and default priors in Table 1. Using these fits instead of the literature values results in an average difference of  $\sim 0.1$  dex higher stellar mass. We find a similar difference in stellar masses between using a non-parametric SFH and an exponentially declining SFH within PROSPECTOR. This difference in mass with assumed SFH is consistent with that characterized for massive  $\log_{10} M_*/M_\odot > 11$  galaxies (Leja et al. 2019b). Our results do not significantly depend on the choice of SFH or its impact on measured stellar mass, which affect our measurements of  $f_{H_2}$  by less than a factor of 1.5.

A second impact of the non-parametric SFH is that the mass-weighted age of the galaxies are typically older than that derived using parametric SFH (Leja et al. 2019b). While the ages measured assuming an exponentially declining model are typically of order 1-3 Gyr, the non-parametric model returns ages of order 2-3 Gyr.

These imply that the major star formation episodes in our sample happened above  $z > 3$ . We list both values in Table 1. In the rest of this work, stellar age will refer to mass-weighted age, and we adopt the older ages from the non-parametric model because it is the more conservative constraint, as we will discuss in Section 4.2.

### 2.1.1. Estimation of the star formation rates

In this work we consider star formation rate (SFR) measured using two different methods, from the SED fitting outlined in the last section, and also that measured by modeling the obscured and unobscured fluxes,  $SFR_{UV+IR} = SFR_{UV,uncorr} + SFR_{IR}$  as published in the UltraVISTA catalog (Muzzin et al. 2013a). The  $SFR_{UV,uncorr}$  is calculated using the conversion of Kennicutt (1998) and the IR component is extrapolated from observed  $24\mu m$  flux following Wuyts et al. (2008). SFRs from either method of SED fitting or extrapolated from  $24\mu m$  are uncertain for quiescent galaxies. In particular, the  $SFR_{UV+IR}$  should be considered an upper limit, because of significant contributions to the mid and far infrared flux that do not trace ongoing star formation in older galaxies (e.g. asymptotic giant branch (AGB) stars, AGN, dust heated by older stars Salim et al. 2009; Fumagalli et al. 2014; Utomo et al. 2014; Hayward et al. 2014). We list the SFR measured using both indicators in Table 1, and in the rest of this work we adopt  $SFR_{UV+IR}$  when measuring sSFR, which we explicitly consider to be an upper limit. Our upper limits to the sample sSFR range from  $-10 < \text{Log}_{10} \text{sSFR} < -12 \text{ yrs}^{-1}$ .

### 2.1.2. Hubble Space Telescope imaging

Our ALMA target selection includes the requirement of high-resolution rest-frame optical imaging from *HST* to enable accurate measurements of morphology of the sample. Because compactness is known to be the strongest predictor of quiescence (Franx et al. 2008; Bell et al. 2012; Teimoorinia et al. 2016; Whitaker et al. 2017) this requirement enables an assessment of a possible additional correlation with gas content. Our selected galaxies are structurally representative for their redshift, spanning a large range of half-light radius ( $R_e$ ) and stellar densities ( $\Sigma_\star \propto M_\star/R_e^2$ ) among quiescent galaxies (Figure 1).

We process all available *HST* imaging covering the ALMA sources with the GRIZLI software<sup>1</sup> (Brammer, in prep.). These include WFC3/F160W imaging from programs 12167, 14114, 12440, and ACS F814W imaging from programs 10092 and 9822. Briefly, we first group all

<sup>1</sup> <https://github.com/gbrammer/grizli>



**Table 1.** Properties of ALMA targets

ID <sup>a</sup>	RA	Dec	$z_{\text{spec}}$	Mass	SFR <sub>UV+IR</sub> <sup>b</sup>	SFR <sub>30Myr</sub> <sup>c</sup>	Re[kpc] <sup>d</sup>	Age <sup>e</sup>	Age <sup>f</sup>	Reference
22260	149.818229	2.561610	1.240	11.51 <sup>+0.04</sup> <sub>-0.03</sub>	3.6	5.3 <sup>+3.41</sup> <sub>-1.91</sub>	7.6	3.4	4.6	Bezanson+2013
20866	149.800931	2.537990	1.522	11.46 <sup>+0.03</sup> <sub>-0.03</sub>	12.8	0.7 <sup>+2.69</sup> <sub>-0.68</sub>	2.4	2.4	1.7	Bezanson+2013
34879	150.131380	2.523800	1.322	11.32 <sup>+0.04</sup> <sub>-0.04</sub>	22.9	1.4 <sup>+2.30</sup> <sub>-1.20</sub>	5.5	2.5	2.1	Belli+2015
34265	150.170160	2.481100	1.582	11.51 <sup>+0.03</sup> <sub>-0.03</sub>	7.4	0.3 <sup>+1.61</sup> <sub>-0.34</sub>	0.9	2.1	1.3	Belli+2015
21434	149.816230	2.549250	1.522	11.39 <sup>+0.03</sup> <sub>-0.03</sub>	19.1	0.5 <sup>+1.79</sup> <sub>-0.49</sub>	1.9	2.1	1.2	Bezanson+2013,2019
307881	150.648487	2.153990	1.429	11.63 <sup>+0.03</sup> <sub>-0.03</sub>	5.0	0.7 <sup>+1.73</sup> <sub>-0.66</sub>	2.7	2.7	3.2	Onodera+2012

<sup>a</sup>We adopt IDs as published in the source reference. ID for galaxy 34265 is from Belli et al. (2015) but is referred to as NMBS-COSMOS18265 in van de Sande et al. (2013).

<sup>b</sup>SFR<sub>UV+IR</sub> values correspond to those published by the ULTRAVISTA survey Muzzin et al. (2013a).

<sup>c</sup>Corresponds to the average SFR over the past 30 Myr as derived from our SED fitting with PROSPECTOR.

<sup>d</sup>Circularized half light radius, defined as  $R_e = r_e \sqrt{b/a}$  where  $r_e$  is the semi-major axis and  $b/a$  is the axis ratio. Measured with GALFIT (Peng et al. 2002)

<sup>e</sup>Mass-weighted stellar age as derived from fitting with non-parametric SFH PROSPECTOR (in Gyr).

<sup>f</sup>Mass-weighted stellar age assuming an exponentially declining SFH (in Gyr).

exposures into associations defined as exposures taken with a single combination of instrument, bandpass filter, and guide-star acquisition (i.e., a “visit” in the standard *Hubble* nomenclature). We align all individual exposures in an association to each other allowing small shifts to the original astrometry from the files downloaded from the MAST archive at STScI. For the global astrometry, we generate a reference astrometric catalog from sources in the ultra-deep optical catalog of the entire COSMOS field provided by the HyperSurprime-Cam Subaru Strategic Program (DR2; Aihara et al. 2019), which we have verified is well aligned to the GAIA DR2 reference frame (Gaia Collaboration et al. 2016, 2018). We align the *HST* association exposures as a group to this reference catalog, allowing for corrections in shift, scale and rotation, resulting in a final global astrometric precision of  $\sim 30$  milli-arcseconds. Finally, we combine exposures in a given filter (from one or more associations) using DRIZZLEPAC / ASTRODRIZZLE (Gonzaga & et al. 2012).

## 2.2. ALMA observations

The ALMA observations of our target galaxies were carried out in project 2018.1.01739.S (PI: Williams) in separate observing sessions from December 18, 2018 to January 17, 2019 using the Band 3 (3 mm) receivers. We combine the results from this program with ALMA data for one similar galaxy from a previous pilot program (2015.1.00853.S; see Bezanson et al. 2019, for details).

The correlator was configured to center the CO(2–1) line within a spectral window of 1.875 GHz width, which

provides  $\sim 5500 \text{ km s}^{-1}$  of bandwidth centered on the expected frequency of the CO line,  $\approx 89.3\text{--}102.9 \text{ GHz}$ . Three additional spectral windows were used for continuum observations. Targets 20866, 22260, and 307881 were observed for a total of  $\sim 90\text{--}100$  min on-source, while 34265 and 34879 were each observed for about twice as long. The array was in a compact configuration yielding synthesized beam sizes  $\sim 1.5\text{--}2.5''$  so as not to spatially resolve the target galaxies. Bandpass and flux calibrations were performed using J1058+0133 and gain calibration using J0948+0022. The data were reduced using the standard ALMA pipeline and the reductions checked manually. Our cleaning procedure involved first masking regions with clearly-detected emission ( $S/N > 5$ ) and then we used a stopping criterion of  $3\times$  the image rms.

Images of both the continuum and line emission were created using natural weighting of the visibilities to maximize sensitivity, with pixel sizes chosen to yield 5–10 pixels across the synthesized beam. The spectral cubes have a typical noise of  $50\text{--}65 \mu\text{Jy/beam}$  in a  $400 \text{ km/s}$  channel measured near the rest-frequency of the CO(2–1) line. The continuum data combined all available spectral windows, and reach a typical sensitivity of  $\sim 5 - 9 \mu\text{Jy/beam}$ , calculated as the rms of the non-primary-beam corrected image. All target galaxies are undetected in the continuum. However, the continuum imaging yielded several serendipitous 3-mm sources in these deep data. Two of these continuum sources

were previously unknown galaxies and are presented in Williams et al. (2019).

### 2.3. Molecular gas measurements

To extract CO(2–1) spectra for each source, we used the *uvmultifit* package (Martí-Vidal et al. 2014) to fit pointlike sources to the visibilities, averaging together channels in order to produce a number of resulting spectra with channel widths ranging from 50–800 km s<sup>−1</sup>. Given the low spatial resolution of the data and the compact galaxy sizes as measured in the available *HST* imaging, the point-like source approximation is likely valid. For most sources, we fixed the position of the point source component to the phase center of the ALMA data, with two exceptions detailed below, leaving only the flux density at each channel as a free parameter. The spectra of each target are shown in Figure 2.

In source 22260, we detect a weak emission line at the correct frequency for the galaxy’s redshift, but offset  $\sim 1.2 \pm 0.3''$  from the expected position of the target galaxy, a marginally-significant offset given the signal-to-noise of these 2'' resolution data. It is not clear if this offset is spurious, due to an astrometric offset with respect to the *HST* imaging (although unlikely given our careful registration to GAIA), or reflective of a more complex physical scenario with a gas-rich region within this galaxy or a very nearby secondary galaxy as has been seen in high-redshift quiescent galaxies (Schreiber et al. 2018). For this source, we fit two point sources to the visibilities, fixing the position of one to the phase center (where we find no detection) and the other to the position of the slightly offset source, which is shown in Figure 2. We subsequently treat this as a real detection of CO(2–1) from our target. As can be seen in the *HST* imaging shown in Figure 2 this galaxy has a secondary optical/near-IR component (seen most prominently at *HST*/ACS 814W shown as inset), possibly indicating a recent minor merger. Deeper high-resolution ALMA data would be necessary to conclusively determine if the origin of the CO(2–1) emission is the secondary optical-IR component.

34879 is a similar scenario, although in that case the line emitter is brighter, offset in velocity from the redshift of our target ( $\Delta v \sim 600$  km/s), and clearly identifiable with a nearby galaxy in the *HST* imaging (Fig. 2). We again extract spectra by fitting multiple point sources to the visibility data for this field, fixing the positions of the sources to the phase center and the observed position of the line emitter, respectively. After this procedure, the spectra extracted at the phase centers of each field show no evidence of CO emission, although we note that the channel fluxes in these spec-

tra are now slightly correlated with the spectra of the offset sources due to the small sky separations compared to the synthesized beam sizes.

For the detected source, 22260, we measure the line flux by fitting a simple Gaussian to the CO(2–1) spectrum. For galaxies that are not detected in CO(2–1), we set upper limits to the line flux. The undetected galaxies have velocity dispersions,  $\sigma$ , measured from the rest-frame optical stellar absorption features in the range  $\sigma \sim 200 - 370$  km s<sup>−1</sup> (Bezanson et al. 2013; Belli et al. 2014) with the exception of 307881 for which it was not measured (Onodera et al. 2012). To measure upper limits to the integrated CO(2–1) line flux of undetected galaxies, we assume similar line widths for the stars as any molecular gas, and adopt typical values for the FWHM of the CO(2–1) of  $2.355 \times \sigma \sim 500$ –600 km s<sup>−1</sup>. We use these line widths and the channel noise to set upper limits on the integrated line fluxes of each target. We note that large linewidths are conservative, and that these upper limits scale with velocity interval  $\Delta v$  as  $\sqrt{\Delta v}$ . Assuming a smaller linewidths would decrease our limiting integrated flux. The CO(2–1) line luminosity for our detected galaxy 22260, and the  $1\sigma$  upper limits in the case of non-detections, are reported in Table 2.

To convert our measurements of CO(2–1) line luminosities into molecular gas mass ( $M_{\text{H}_2}$ ), we make the following standard assumptions about the molecular gas conditions. We first assume a CO excitation (namely the luminosity ratio between the CO(2–1) and CO(1–0) transitions,  $r_{21}$ ) following observations from the local Universe. Although local galaxies with low sSFR are observed to exhibit a range of values  $r_{21} = 0.7 - 1$  (e.g. Saintonge et al. 2017), bulges and the central nuclei of galaxies that are thought to be similar to high-redshift compact quiescent galaxies exhibit near-thermalized excitation,  $r_{21} = 1$  (e.g. Leroy et al. 2009). For our analysis we assume  $r_{21} = 0.8$  following Spilker et al. (2018), which results in more conservative (higher) molecular gas mass measurements and limits than the assumption of thermalized emission. For comparisons to other measurements in the literature of  $z > 1$  passive galaxies we therefore rescale other values to this excitation as  $M_{\text{H}_2} \times (0.8/r_{21})$  (including the object from Bezanson et al. (2019) which we convert to our value of  $r_{21} = 0.8$ ). Assuming a larger value for  $r_{21}$  (e.g. 1, as is done for other studies of passive systems across redshifts) does not significantly change our results, and instead would imply even lower molecular gas fractions that further strengthen our conclusions. This assumption has a minimal impact on our  $M_{\text{H}_2}$  uncertainty budget (10–20%) compared to e.g. a factor of  $\gtrsim 2$  uncertainty due to the

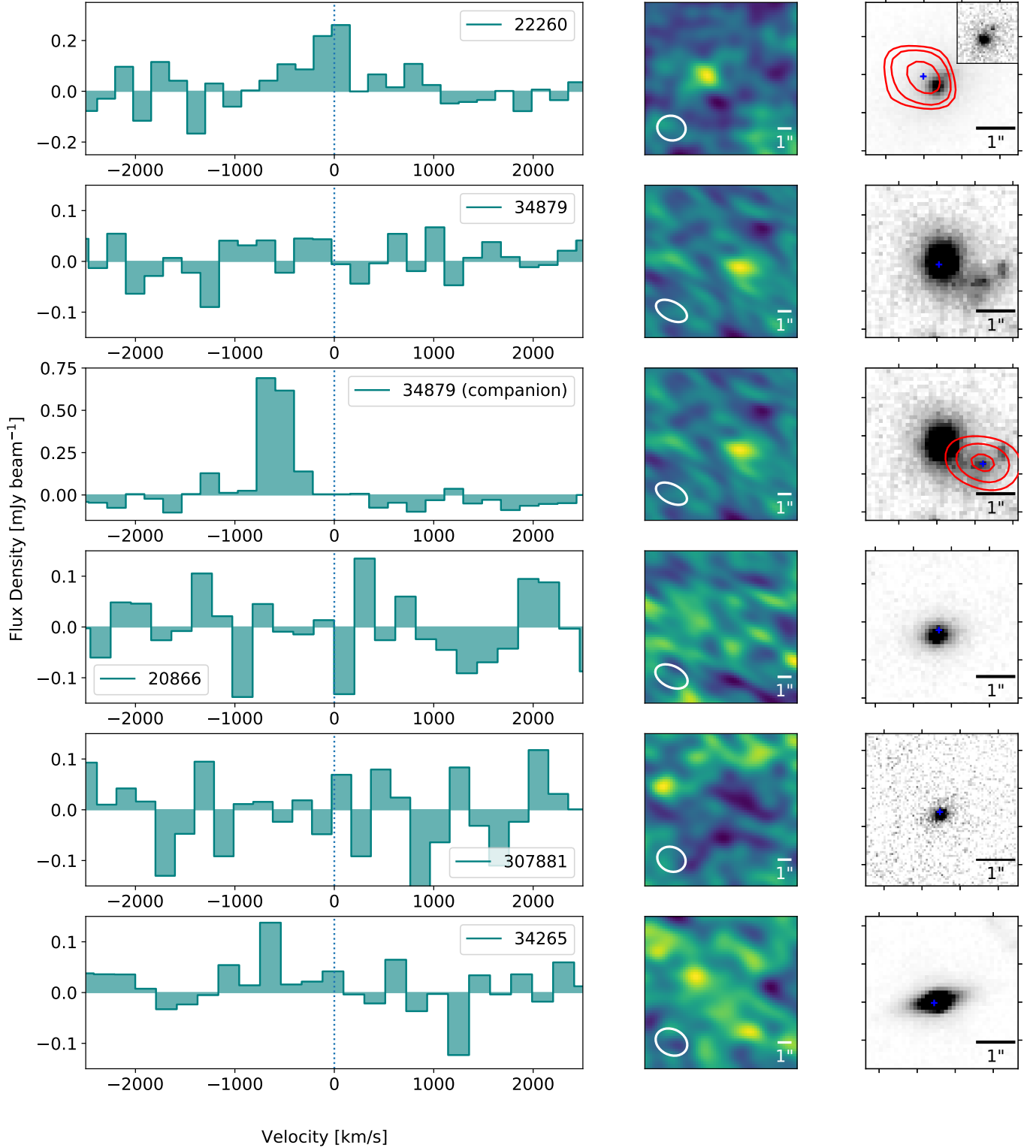


**Figure 2.** Left panel: ALMA CO(2-1) spectra in 200 km/s channels for each of our galaxies. Spectra are extracted from the position of the blue cross in right panel. Middle panel: The ALMA CO(2-1) integrated image in 400 km/s channels centered at CO(2-1) of the target galaxy (except 22260 which shows the integrated image in a 500 km/s channel, where we find a  $4\sigma$  detection; we assume the flux as originating in our source). ALMA beam is indicated by white ellipse. Right panel: the *HST*/WFC3 F160W image for each of our targets. For 22260 we show a zoomed inset of the ACS/F814W imaging where a secondary stellar component is more visible than F160W. We show the CO(2-1) contours in red (where detected). For 22260 we show 50, 60 and 80 mJy/beam km/s contours. For 34879 we show 100, 120 and 130 mJy/beam km/s contours in a 200 km/s channel, offset in velocity from our target galaxy by  $dv=-600$  km/s to show the emission of the companion galaxy. 34879 itself is not detected in CO(2-1).

**Table 2.** Molecular gas properties

ID	$S_\nu^{a,b}$	$S_\nu dv^b$	$L'CO(2-1)^b$	$M_{H_2}^c$	$f_{H_2}^c$
	$\mu Jy$	$mJy \text{ kms}^{-1}$	$10^8 \text{ K km s}^{-1} \text{ pc}^2$	$10^9 \text{ Msun}$	%
22260 <sup>d</sup>	$180 \pm 38$	$90 \pm 19$	$19 \pm 4$	$10.5 \pm 2.2$	$3.2 \pm 0.7$
20866	47.4	23.7	7.5	12.3	$< 4.3$
34879 <sup>d</sup>	27.5	13.8	3.3	5.5	$< 2.6$
34265 <sup>d</sup>	35.1	17.6	5.9	9.8	$< 3.0$
21434	69.6	34.8	8.0	13.7	$< 5.5$
307881	37.8	18.9	5.3	8.8	$< 2.1$
Stack	-	$10.3^e$	2.89	4.7	$< 1.6$

<sup>a</sup>Line flux is measured in a 500km/s channel.

<sup>b</sup>1 $\sigma$  upper limits

<sup>c</sup>3 $\sigma$  upper limits, and assuming  $r_{21} = 0.8$  in temperature units,  $\alpha_{CO} = 4.4$ . Molecular gas masses can be rescaled under different assumptions as  $M_{H_2} \times (0.8/r_{21})(\alpha_{CO}/4.4)$

<sup>d</sup>OII $\lambda$ 3727 detected in emission with Keck.

<sup>e</sup>Assumes 400 km/s bin. Can be scaled to width 500 km/s by multiplying by  $\sqrt{500/400}$ .



assumed value of the CO-H<sub>2</sub> conversion factor to translate the measured CO luminosity to  $M_{\text{H}_2}$ .

In this work we assume a Milky Way like value of  $\alpha_{\text{CO}} = 4.4 \text{ M}_\odot (\text{K km s}^{-1} \text{pc}^2)^{-1}$ , which is a reasonable assumption for massive galaxies with presumably high metallicities (e.g. Narayanan et al. 2012b; see also the review by Bolatto et al. 2013).

#### 2.4. Stack of non-detections in CO(2–1)

With five out of six galaxies undetected in CO(2–1) (including 21434; Bezanson et al. 2019), we perform a stacking analysis of the five non-detected galaxies. We calculate the weighted average (mean) to account for the slight differences in map rms, and use the non-primary beam corrected maps, which have Gaussian noise properties. Since the nearby companion of galaxy 34879 has significantly detected CO(2–1) emission offset by 600 km/s, but with roughly width of 200 km/s, we restrict our exploration of stacked CO(2–1) emission using image cubes with velocity resolution  $\lesssim 400$  km/s to prevent the flux from the companion entering the stack, given the companion’s location within 1.5” of the target galaxies in the stack. We construct image cubes at 400km/s velocity resolution centered at the rest-frequency of CO(2–1) of each galaxy, and stack the velocity bin that contains the CO(2–1) line.

We do not detect any CO(2–1) from the stack of individually undetected sources, with an rms noise limit of  $25.6 \mu\text{Jy/beam}$  for the 400 km/s channel width of the stack. We use the mean redshift of the non-detected galaxies ( $\langle z \rangle = 1.476$ ) to put a  $1\sigma$  upper limit to the average CO luminosity of  $L'_{\text{CO}(2-1)} < 2.9 \times 10^8 \text{ K km s}^{-1} \text{ pc}^2$ . We make the same assumptions listed in Section 2.3 to convert this measurement to a molecular gas mass and find  $M_{\text{H}_2} < 4.7 \times 10^9 \text{ M}_\odot$  ( $3\sigma$ ). Using the average stellar mass of our undetected sample of  $\log_{10} M_*/\text{M}_\odot \sim 11.5$ , this puts a  $3\sigma$  upper limit on the molecular gas fraction of 1.6%. The stacked sample has an average specific star formation rate of  $6 \times 10^{-11} \text{ yr}^{-1}$  (likely an upper limit, as explained in Section 2.1.1) and the properties derived from the stack are summarized in Table 2.

### 3. RESULTS

Our new ALMA observations indicate that our sample of massive ( $\log_{10} M_*/\text{M}_\odot > 11.3$ ) and quiescent ( $\log_{10} \text{sSFR} \lesssim -10 \text{ yr}^{-1}$ ) galaxies at  $z > 1$  have low molecular gas masses ( $M_{\text{H}_2} \lesssim 5 - 10 \times 10^9 \text{ M}_\odot$ ), translating to molecular gas fractions ( $f_{\text{H}_2} = M_{\text{H}_2}/M_*$ ) between  $\sim 2\text{--}6\%$ . To provide context for these measurements, we compile measurements of molecular gas using CO as a tracer from the literature across redshifts. We include surveys that target low-J transitions ( $J_{\text{up}} \lesssim 2$ )

to minimize uncertainties from variations in the methods to correct for CO excitation. The majority of these surveys targeted star forming galaxies outside the local Universe, including PHIBSS (Tacconi et al. 2013), PHIBSS2 (Tacconi et al. 2018; Freundlich et al. 2019), as well as smaller programs targeting Milky-Way progenitors (Papovich et al. 2016), extended disk galaxies (Daddi et al. 2010), compact star-forming galaxies (Spilker et al. 2016), and galaxies from overdense regions (Hayashi et al. 2018; Rudnick et al. 2017). To targeted samples, we add CO-detected sources from the blind ASPECS Survey (Decarli et al. 2016; Aravena et al. 2019). We also include the few studies that have targeted quiescent or post-starburst galaxies outside the local universe at  $z < 1$  (Suess et al. 2017; Spilker et al. 2018). Finally we include the large surveys at  $z \sim 0$  that have enabled an exploration of molecular gas in similarly massive galaxies to our sample, at similarly low sSFRs (albeit at late cosmic times; Young et al. 2011; Saintonge et al. 2012, 2017; Davis et al. 2016).

To date, molecular gas measurements using CO exist for only two confirmed quiescent galaxies above  $z > 1$ ; these are upper limits ( $3\sigma$ ) on a massive quiescent galaxy published by Sargent et al. (2015,  $f_{\text{H}_2} \lesssim 13\%$ , converted from Salpeter IMF) and the pilot galaxy for this survey ( $f_{\text{H}_2} \lesssim 5.5\%$ ; Bezanson et al. 2019, using our derived stellar mass and velocity width, to be consistent with the rest of the sample). Both measurements are rescaled to our assumption  $r_{21}=0.8$ . Both galaxies are spectroscopically confirmed, enabling a robust upper limit to their molecular gas content.

The most comprehensive constraint on the average molecular gas in quiescent galaxies at  $z > 1$  to date is a far-infrared stack of 977 photometrically selected quiescent galaxies (Gobat et al. 2018), where the molecular gas content is inferred from the average dust emission (Magdis et al. 2012). We add this measurement to the CO constraints from the literature because it uses the largest sample of quiescent galaxies at  $z > 1$ .

Figures 3 and 4 show  $f_{\text{H}_2}$  for our sample as a function of sSFR and  $M_*$ . We plot our ALMA measurements as stars, along with the measurements from the literature (small translucent symbols). Quiescent galaxies at  $z > 1$  are large bold symbols. We additionally include the stacked measurement from the five non-detected galaxies (diamond). Figure 3 shows that based on our deep limits, massive and quiescent galaxies at  $z > 1$  have comparably low gas fractions relative to galaxies at  $z = 0$  with similar sSFRs, and that our deep  $f_{\text{H}_2}$  limits are comparable to local surveys. Figure 4 shows that our upper limits on  $f_{\text{H}_2}$  are the lowest CO-derived constraints

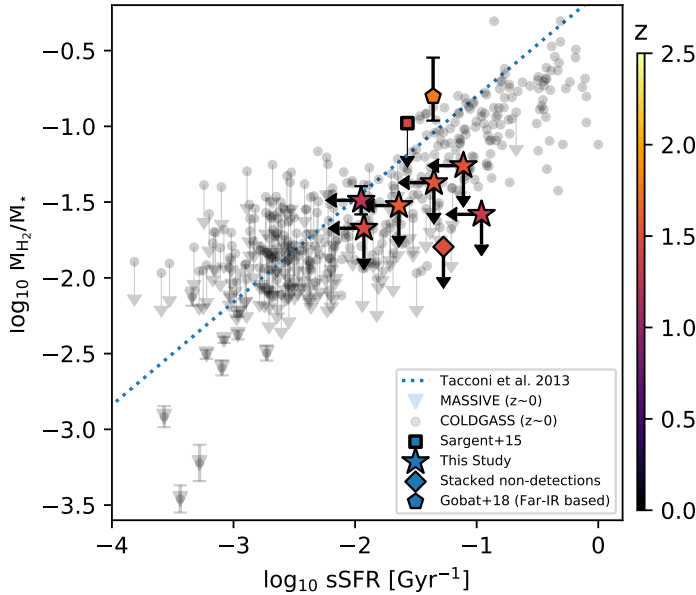


**Figure 3.** Comparison of our CO measurements to those of quiescent galaxies at  $z \sim 0$  from the COLDGASS and MASSIVE surveys (Saintonge et al. 2017; Davis et al. 2016). Large symbols indicate quiescent galaxies at  $z > 1$  (this work; Sargent et al. 2015; Bezanson et al. 2019) and the far-infrared based stack of Gobat et al. (2018). Our sample has low  $f_{\text{H}_2} < 2 - 6\%$ ; comparably low to galaxies at  $z=0$  with similarly low sSFR.

on molecular gas content of any galaxy population above  $z > 1$ .

The left panel of Figure 4 shows  $f_{\text{H}_2}$  vs sSFR at  $z > 0$ , with galaxies color coded by redshift. The gas fraction measurement/limits for our sample are about an order of magnitude deeper than the limit set by Sargent et al. (2015), and an order of magnitude lower than that inferred from dust emission by Gobat et al. (2018). We discuss this discrepancy in quiescent galaxy  $f_{\text{H}_2}$  between their average detection and our deep limits further in Section 4.1.

In the right panel, we plot  $f_{\text{H}_2}$  vs stellar mass, where galaxies are again color coded by redshift. Our measurements are in line with observations that the gas fraction in galaxies decreases with increasing stellar mass at all redshifts, although the mass dependence is weak compared to the stronger dependencies on redshift and sSFR (e.g. Tacconi et al. 2018). Our study doubles the number of constraints on molecular gas mass at  $z > 1$  at the massive ( $\log_{10} M_*/M_\odot > 11.3$ ) end.

In Figure 5 we plot  $f_{\text{H}_2}$  as a function of redshift, where galaxies are color coded by sSFR. A number of well-known scaling relations are apparent in Figures 3, 4, and 5 including that overall, the molecular gas fractions in galaxies decrease with decreasing redshift, decreasing

sSFR, and increasing stellar mass. Our data contributes new datapoints to the poorly explored parameter space at low sSFR, high mass, at high redshift.

#### 4. DISCUSSION

In this paper, we have placed constraints on the molecular gas content in the first sample of massive quiescent galaxies at  $z > 1$  ( $< z \leq 1.45$ ). Our low  $f_{\text{H}_2}$  measurements indicate that the exhaustion or destruction of molecular gas in massive quiescent galaxies is efficient and complete, consistent with the finding for our pilot galaxy (Bezanson et al. 2019). That massive quiescent galaxies at  $z > 1$  are gas poor suggests high star-formation efficiency and rapid depletion times during their evolution. While our sample is not complete in stellar mass, we do not find evidence within our sample that  $f_{\text{H}_2}$  varies with either galaxy size or surface density  $\Sigma_*$ . Among quiescent galaxies, these structural properties are known to correlate with stellar age (e.g. Williams et al. 2017), formation redshift (e.g. Estrada-Carpenter et al. 2020) and quenching timescale (e.g. Belli et al. 2019), and therefore plausibly trace timescales for gas consumption. We measure  $f_{\text{H}_2} < 2 - 6\%$ , values that are universally low despite the large dynamic range of structure we probe among quiescent galaxies at  $z > 1$  ( $R_e = 0.9 - 7$  kpc;  $\log_{10} \Sigma_* = 8.9 - 10.8$   $M_\odot \text{ kpc}^{-2}$ ; Figure 1).<sup>2</sup>

Our sample suggests that massive galaxies that cease star formation at the peak epoch of quenching do not retain large reservoirs of gas. These findings are in contrast with observations of recently quenched galaxies at  $z < 1$ , some of which contain significant molecular gas reservoirs ( $f_{\text{H}_2} \sim 20 - 30\%$ ), suggesting that their low SFRs are due to decreased star-formation efficiency (e.g. suppressed dynamically) rather than a lack of fuel for star-formation (Rowlands et al. 2015; French et al. 2015; Suess et al. 2017; Smercina et al. 2018; Li et al. 2019). Furthermore, Spilker et al. (2018) find  $f_{\text{H}_2} < 1 - 15\%$  in quiescent galaxies at intermediate redshifts ( $z \sim 0.7$ ), additional evidence for heterogeneity among galaxies below the main sequence. Our new results, collectively with those at  $z < 1$ , highlight a diversity in molecular gas properties among quenching galaxies across cosmic time, possibly indicating that the primary drivers of quenching change over cosmic time. These new observations of the variation in gas reservoirs of non-starforming galaxies across cosmic time are therefore important constraints for our theoretical formulations of quenching processes, and the time evolution of gas reservoirs. In

<sup>2</sup> We note that quiescent galaxies are generally higher  $\Sigma_*$  than star forming galaxies, which have larger gas reservoirs.

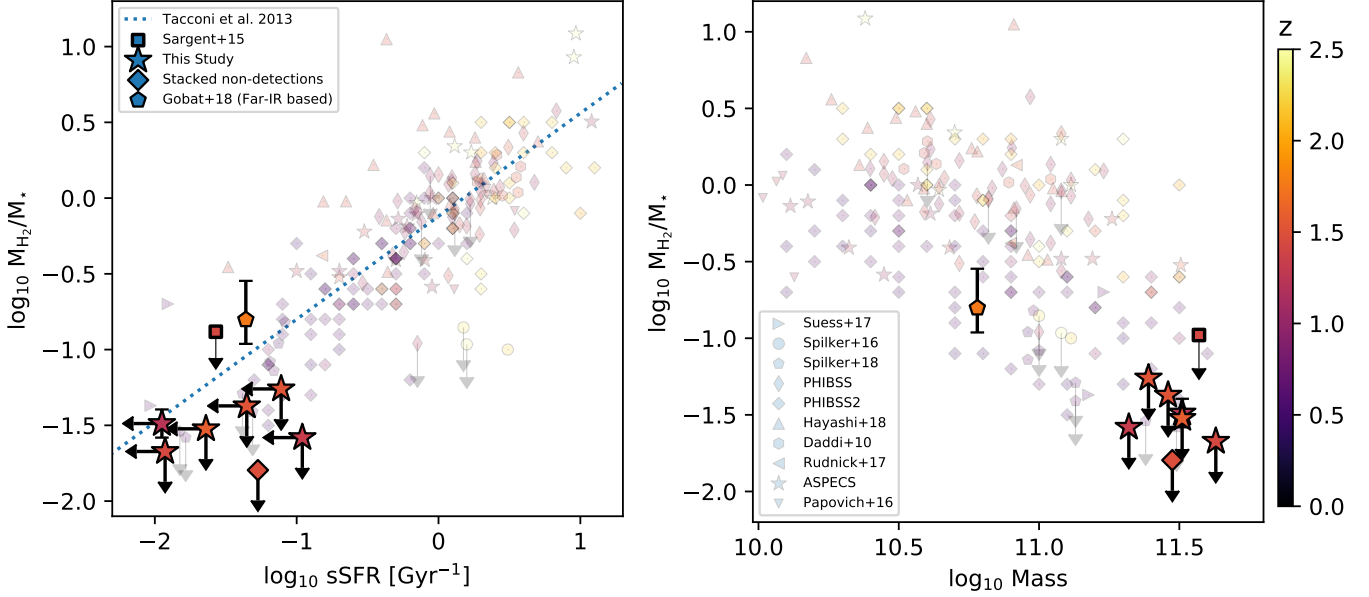


**Figure 4.** Comparison of our measurements to measurements based on CO in literature at  $z > 0.5$ . Large symbols indicate quiescent galaxies at  $z > 1$  (this work; Sargent et al. 2015; Bezanson et al. 2019) and the far-infrared based stack of Gobat et al. (2018). Small symbols (defined in right panel legend) indicate comparison literature measurements. Our sample have low molecular gas fraction  $< 2 - 6\%$ ; 1-2 orders of magnitude lower than few coeval star-forming galaxies at similar stellar mass.

the following sections, we explore the implications of our new low gas fraction measurements in this context.

#### 4.1. The distribution (intrinsic scatter) of cold gas content among $z > 1$ quiescent galaxies

Although this is the first systematic study using CO to measure molecular gas in quiescent galaxies at  $z > 1$ , the recent observation of average far-IR properties of 977 quiescent galaxies at  $z > 1$  found significant dust continuum emission, implying a relatively large molecular gas content ( $f_{\text{H}_2} \sim 16\%$  when converted to Chabrier IMF; Gobat et al. 2018). The individual measurements of molecular gas in our quiescent sample range from  $f_{\text{H}_2} \lesssim 2-6\%$ , and are inconsistent with the average  $f_{\text{H}_2}$  measurement by Gobat et al. (2018). While a primary uncertainty in our  $f_{\text{H}_2}$  measurement is the assumed value of  $\alpha_{\text{CO}}$ , extreme values only observed in low mass and low metallicity systems ( $\alpha_{\text{CO}} \gtrsim 15$ ; Bolatto et al. 2013; Narayanan et al. 2012b) would be required to bring our measurements into agreement.

A direct comparison to the Gobat et al. result is difficult owing in part to our differing methodologies, each of which is subject to its own systematic uncertainties. And, as with any photometric selection of quiescent galaxies, there is always some risk of contamination from dusty star-forming galaxies. The contamination may enter the stack either through misidentification because of the age-dust degeneracy of colors (even if only a few bright objects), or due to neighboring dusty galaxies given the low spatial resolution of the far-IR data ( $\sim 10$ -

30"). Neighbors can contaminate either through poor source subtraction, or as hidden dusty galaxies that do not appear in optical/near-IR selection but may remain within the far-IR photometric beam (e.g. Simpson et al. 2017; Schreiber et al. 2018; Williams et al. 2019). Further, both our sample and dusty star forming galaxies are massive and may be strongly clustered (e.g. Hickox et al. 2012, although see also Williams et al. 2011). In this section we ignore any such possible contamination, and discuss several physical explanations for this disagreement.

First, the relatively large  $f_{\text{H}_2}$  observed by Gobat et al. (2018) could be reflecting a heterogeneity of molecular gas properties among the passive galaxy population at  $z > 1$ , as is observed at  $z < 1$ . Our sample represent some of the most massive and oldest passive galaxies known at  $1 < z < 1.5$ , while the Gobat et al. 2018 sample is dominated by objects less massive than our sample ( $< \log_{10} M_* \geq 10.8$ ). Perhaps lower mass and/or younger additions to the red sequence still have molecular gas leftover, contributing to the far-IR emission observed on average. However, we note that because the stack is average, and our measurements are  $> 10\times$  lower  $f_{\text{H}_2}$ , a heterogenous sample would imply even larger  $f_{\text{H}_2} > 16\%$  in any sample of gas-rich quiescent galaxies. More surveys that span a larger range of parameter space for individual quiescent galaxies (e.g. lower mass) are required to investigate this explanation further (Whitaker et al. in prep, Caliendo et al. in prep).

Alternatively, the calibration to convert the far-IR emission into a measurement of  $M_{\text{H}_2}$  might not be universal. These conversions are typically based on assumed dust to gas ratios and/or dust temperatures, calibrated using primarily star-forming galaxies (e.g. Magdis et al. 2012; Scoville et al. 2016). In theory this relies on an intrinsic relationship between dust and gas content that has been shown to accurately describe star forming galaxies (Kaasinen et al. 2019), and for the most part, also holds for quiescent galaxies in the local Universe, albeit with large scatter (e.g. Lianou et al. 2016). In principle, dust traces both atomic (HI) and molecular ( $\text{H}_2$ ) gas phases, and so this could still hold if the HI/ $\text{H}_2$  ratio is high in quiescent galaxies, while the dust to  $\text{H}_2$  ratio is very low. We note that Spilker et al. (2018) stacked the 2mm dust continuum emission to compare to  $M_{\text{H}_2}$  measured from CO, finding consistent values between  $M_{\text{H}_2}$  observed via CO and dust, lending support for the idea that dust to  $\text{H}_2$  conversions hold for massive quiescent galaxies at high redshift. However, Gobat et al. (2018) make the simplifying assumption that all gas traced by dust is molecular, although HI/ $\text{H}_2$  mass ratios in local quiescent galaxies can be large (Zhang et al. 2019) and diverse (Welch et al. 2010; Young et al. 2014; Boselli et al. 2014; Calette et al. 2018). It is therefore a possibility that the significant dust emission detected by Gobat et al. (2018) is not in conflict with our low  $f_{\text{H}_2}$  measurements, and instead is primarily tracing atomic HI rather than  $\text{H}_2$ .

Nevertheless, other factors may affect these conversions, warranting further exploration. For example the dust to gas ratio can also vary with metallicity, as explored in simulations, although the extent to which this disrupts scaling relations is not clear (i.e. gas/dust may plateau above solar metallicity, applicable to most massive galaxies; Privon et al. 2018; Li et al. 2019). Future samples of quiescent galaxies with observations of both CO and dust continuum emission would reveal if the dust to  $M_{\text{H}_2}$  calibrations apply across galaxy populations at high redshift, as done locally (Smith et al. 2012). The comparison between our work presented here and that presented in (Gobat et al. 2018) thus highlights several avenues of future investigation to understand the intrinsic scatter in molecular gas properties of quiescent galaxies, which will help understand the diversity of pathways that passive galaxies may take to quiescence.

#### 4.2. Timescales for gas consumption or destruction

Accretion is now considered to be a primary driver of galaxy growth in the early Universe (for a review see Tacconi et al. 2020). While observations support this

picture, it remains unclear what disrupts the growth in massive galaxies that become quiescent. Explanations include the destruction or expulsion of gas due to feedback, the suppression of gas accretion (e.g. by virial shocks once  $\log_{10} M_{\text{halo}}/M_{\odot} > 12$ ), or the suppression of gas collapse due to the development of a stellar bulge. Our observations of molecular gas in quenched galaxies can help discriminate between the different processes. In particular, we explore here the timescales for gas expulsion or consumption that are consistent with the low gas fractions we measure. Unfortunately with mostly upper limits to  $M_{\text{H}_2}$ , and likely only upper limits to the SFR, our dataset precludes a robust measurement of (current) depletion times ( $t_{\text{dep}} = M_{\text{H}_2}/\text{SFR}$ ) and we instead explore the allowable range of  $t_{\text{dep}}$  given low  $f_{\text{H}_2}$  and old mass-weighted stellar age.

##### 4.2.1. Closed-box toy model: constant $t_{\text{dep}}$

To provide qualitative insight into the timescales required to achieve the low  $f_{\text{H}_2}$  we observe, we construct a closed-box toy model for a  $\log_{10} M_*/M_{\odot} \sim 11$  main sequence galaxy that stops gas accretion, and then depletes its existing gas reservoir at specified depletion times. The SFR is decreased accordingly as gas is consumed. This model is qualitatively similar to that used in Spilker et al. (2018) to investigate if their measured depletion times for quiescent galaxies at  $z \sim 0.7$  are consistent with depleting to levels observed in quiescent galaxies at  $z = 0$ .

We first assume a toy model with a constant  $t_{\text{dep}}$  that remains the same with time and SFR, and calculate how the gas fraction declines if the gas accretion is halted while the galaxy is on the main sequence at  $z = 2, 3, 4$ . We additionally assume that as the galaxy consumes its gas through star formation, stellar mass loss will return  $\sim 30\%$  of that mass back to the interstellar medium (ISM; for a Chabrier IMF; e.g. Leitner & Kravtsov 2011; Scoville et al. 2017). While this is a physically motivated assumption, it also is conservative. If the true fraction of gas returned to the ISM is lower, the gas reservoir will be depleted even faster, strengthening our conclusions.

In the left panel of Figure 5, the blue curves show the evolution of these constant  $t_{\text{dep}}$  closed box models at  $z = 2, 3, 4$  for  $t_{\text{dep}} = 0.3, 0.5, 0.6$  Gyr, respectively. The higher the redshift that accretion is halted, the longer the limiting  $t_{\text{dep}}$  that is consistent with our low gas fractions. Longer depletion times will flatten the blue curves and are inconsistent with our measurements. These curves indicate that rapid depletion times are required for a main sequence galaxy to use up its existing reservoir if accretion is halted. The earlier in cosmic time the accretion is halted, the longer  $t_{\text{dep}}$  can be



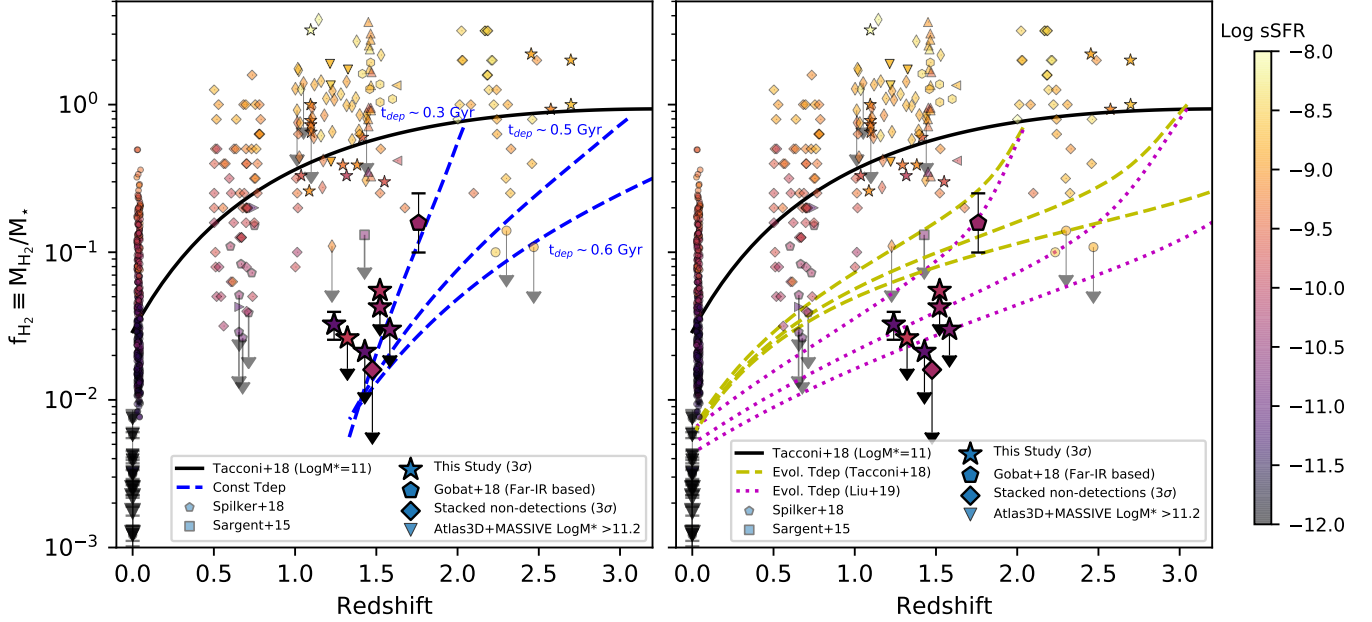


**Figure 5.**  $f_{\text{H}_2}$  vs redshift for galaxies in our sample (large stars) and literature measurements. All galaxies are color-coded by their sSFR. Symbols are represented as in Figure 4. For clarity we omit  $z = 0$  measurements below  $f_{\text{H}_2} < 10^{-3}$  from the Atlas3D or MASSIVE surveys, and two measurements above  $f_{\text{H}_2} > 5$  at  $z \sim 2$  from (Hayashi et al. 2018). Black line indicates the  $f_{\text{H}_2}$  on the main sequence for star forming galaxies with  $\log_{10} M_*/M_\odot = 11$ . Lines show the gas depletion according to our toy models outlined in Section 4.2: blue curves indicate models with constant  $t_{\text{dep}} = 0.3, 0.5, 0.6$  Gyr where accretion halts at  $z = 2, 3, 4$ , respectively. Yellow indicate models where the value of  $t_{\text{dep}}$  changes according to scaling relations measured by Tacconi et al. (2018). Our low gas fractions require rapid  $t_{\text{dep}}$ , inconsistent with Tacconi et al. (2018), and have better agreement with relations that have faster depletion times at high redshift, low sSFR, and high mass (Liu et al. 2019, magenta curves).

and still match our observations. However we note that for mass-weighted ages of  $\sim 1\text{--}3$  Gyr (all galaxies except 22260<sup>3</sup>), the majority of star-formation occurred before  $z = 3.5$ , indicating a limiting  $t_{\text{dep}} < 0.6$  Gyr. This is also roughly the typical depletion times for massive galaxies on the main sequence at these redshifts ( $\sim 0.4\text{--}0.6$  Gyr Tacconi et al. 2018; Liu et al. 2019). Our data is consistent with this simple picture where galaxies truncate accretion and then consume the existing gas at typical main sequence  $t_{\text{dep}}$  rates, or faster.

#### 4.2.2. Closed-box toy model: varying $t_{\text{dep}}$

While the constant  $t_{\text{dep}}$  toy model is useful for providing the qualitative intuition that long depletion timescales ( $t_{\text{dep}} > 0.6$  Gyr) are inconsistent with our data, observations have shown that in reality,  $t_{\text{dep}}$  is not constant as galaxies evolve.  $t_{\text{dep}}$  is known to vary as a function of redshift, sSFR (i.e. distance from the main sequence), with weaker dependences on  $M_*$  and galaxy size (Tacconi et al. 2013; Santini et al. 2014; Genzel et al.

2015; Tacconi et al. 2018; Liu et al. 2019; Tacconi et al. 2020). Therefore, we also explore a closed box model where the  $t_{\text{dep}}$  smoothly evolves according to scaling relations as galaxies leave the main sequence. These scaling relations imply an increase in  $t_{\text{dep}}$  as galaxies move below the main sequence, which slows the rate that  $f_{\text{H}_2}$  decreases with time. For this set of toy models we make the conservative, albeit unrealistic, assumption that no mass is returned by stars to the ISM as galaxies move below the main sequence. This is the more conservative comparison in this case, because any mass loss to the ISM during this phase will increase the time required for the toy model to reach the low  $f_{\text{H}_2}$  we observe.

The right panel of Figure 5 shows the result of this toy model calculation for two example scaling relations, that of Tacconi et al. (2018) in yellow and of Liu et al. (2019) in magenta. In the case of Tacconi et al. (2018), the simple consumption of gas does not reach low enough gas fractions quickly enough to match our observations. This is due to the relatively long depletion times below the main sequence implied by this particular scaling relation. This is not necessarily surprising, as primarily star-forming galaxies are used to calibrate these rela-

<sup>3</sup> We note the possibility that 22260 received its gas later through a minor merger from its secondary component, and therefore its older age does not disagree with this picture.



tions outside the local Universe; understanding the evolution of the star-forming population was the primary goal of these analyses. Scaling relations measured in Genzel et al. (2015); Tacconi et al. (2020) result in similar behavior.

Taken at face value, the Tacconi et al. (2018) relation implies that  $t_{\text{dep}} = 0.7, 0.6, 0.5$  Gyr for a  $\log_{10} M_*/M_\odot = 11$  galaxy leaving the main sequence at  $z=2,3,4$ , as explored in Figure 5. Extrapolating the relation to the average mass, sSFR and redshifts of our ALMA targets would imply  $t_{\text{dep}} \sim 1.6$  Gyr and  $f_{\text{H}_2} \sim 10\%$ . For the ALMA galaxies individually, the relation implies  $f_{\text{H}_2}$  values that are  $> 2\times$  larger than our conservatively measured  $3\sigma$  upper limits. Our data safely rule out these extrapolations.

In contrast, the closed box model based on scaling relations measured by Liu et al. (2019) reaches substantially lower  $f_{\text{H}_2}$ . This is primarily due to a more rapid  $t_{\text{dep}}$  near but below the main sequence at high redshift in their calibration, compared to the behavior of  $t_{\text{dep}}$  measured by Tacconi et al. (2018). As is apparent, the faster  $t_{\text{dep}}$  near but below the main sequence has a substantial impact on the behavior of our toy model. Therefore, we cannot rule out that our low  $f_{\text{H}_2}$  are consistent with simple gas consumption with behavior similar to Liu et al. (2019) if accretion onto galaxies is halted. However, we note that including physically motivated gas recycling from stellar mass loss as in the last section would drastically increase the time required to reach our measured  $f_{\text{H}_2}$ , and increasing the tension with our observations (30% gas recycling as assumed in the previous section results in the  $z = 4$  magenta curve consistent with only our two highest  $f_{\text{H}_2}$  constraints, too high to explain all our measurements. The  $z = 2 - 3$  curves would be inconsistent with all of our data).

At face value, the Liu et al. (2019) relation implies that  $t_{\text{dep}} = 0.5, 0.4, 0.3$  Gyr for a  $\log_{10} M_*/M_\odot = 11$  galaxy leaving the main sequence at  $z=2,3,4$ , as explored in Figure 5. Extrapolating to the properties of our ALMA targets would imply longer  $t_{\text{dep}} \sim 2.6$  Gyr and lower  $f_{\text{H}_2} \sim 6\%$ , closer to our observations but still  $\sim 4\times$  larger than our stacked result.

We note that our  $3\sigma$  upper limits and our assumption about  $r_{21}$  are conservative, and thus the real gas fractions are likely much lower than the figure suggests. Therefore, we speculate that  $t_{\text{dep}}$  must remain rapid, in disagreement with extrapolations from scaling relations, as galaxies move below the main sequence. Unfortunately, our toy model is highly sensitive to the form of scaling relations at high masses, high redshifts, and below the main sequence, which is poorly explored parameter space. This highlights the need for further ex-

ploration of gas reservoirs in galaxies below the main sequence in the early Universe.

Our finding that scaling relations do not describe galaxies below the main sequence (at least outside of the local Universe) is in agreement with findings by Spilker et al. (2018). Half of their sample (the half with higher  $\log_{10} \text{sSFR} > -1.2$  Gyr and lower mass  $\log_{10} M_*/M_\odot \lesssim 11$ ) was detected in CO with  $f_{\text{H}_2} \sim 7-15\%$ , in agreement with scaling relations. However, the  $f_{\text{H}_2}$  limits measured in their non-detected sample (with similar sSFR and  $M_*$  to our sample) were significantly lower than the expectations based on scaling relations. Both our data and that of Spilker et al. (2018) indicate that scaling relations for the star-forming population don't extrapolate to populations with lower sSFR, and break down around 3 – 5 times below the main sequence (Spilker et al. 2018). Rather,  $t_{\text{dep}}$  likely remains short below the main sequence until gas is used and destroyed, and what little is left cannot be efficiently converted into stars, thereby increasing  $t_{\text{dep}}$ .

Despite the uncertainty in behavior of scaling relations below the main sequence at high-redshift, these comparisons are useful because they qualitatively indicate that  $t_{\text{dep}}$  must be rapid when galaxies are shutting off their star-formation. These conclusions are the same whether we assume the galaxy originates on the main sequence or in a starburst phase (with even faster typical  $t_{\text{dep}}$ ; e.g. Silverman et al. 2015, 2018). Smoothly evolving models of departure from the main sequence where star-formation efficiency is decreased and  $t_{\text{dep}}$  is increased (i.e. reservoirs of gas exist but do not form stars) are inconsistent with our observations.

Finally, we note the possibility that  $t_{\text{dep}}$  evolution is not smooth, and an initial rapid drop in gas fraction due to, e.g. increased star formation efficiency or feedback as galaxies go below the main sequence, is followed by an extended period of low  $f_{\text{H}_2}$  and long  $t_{\text{dep}}$ . That long depletion times kick in after most gas is gone is also consistent with simulations presented by Gensior et al. (2020) that indicate that suppression of star formation efficiency (i.e. lengthening of  $t_{\text{dep}}$ ) due to dynamical stabilization by growth of a bulge in galaxies below the main sequence has an impact only at low  $f_{\text{H}_2}$  ( $< 5\%$ ; see also Martig et al. 2009, 2013). Such a scenario implies an even faster initial depletion of gas than we model here. Therefore, the  $t_{\text{dep}}$  values derived for our sample from these toy models should be considered upper limits.

#### 4.3. Comparison to analytic bathtub models

Further insight is possible by comparing to analytical “bathtub” models, where the gas content of galaxies is an equilibrium of gas infow, outflow and consump-

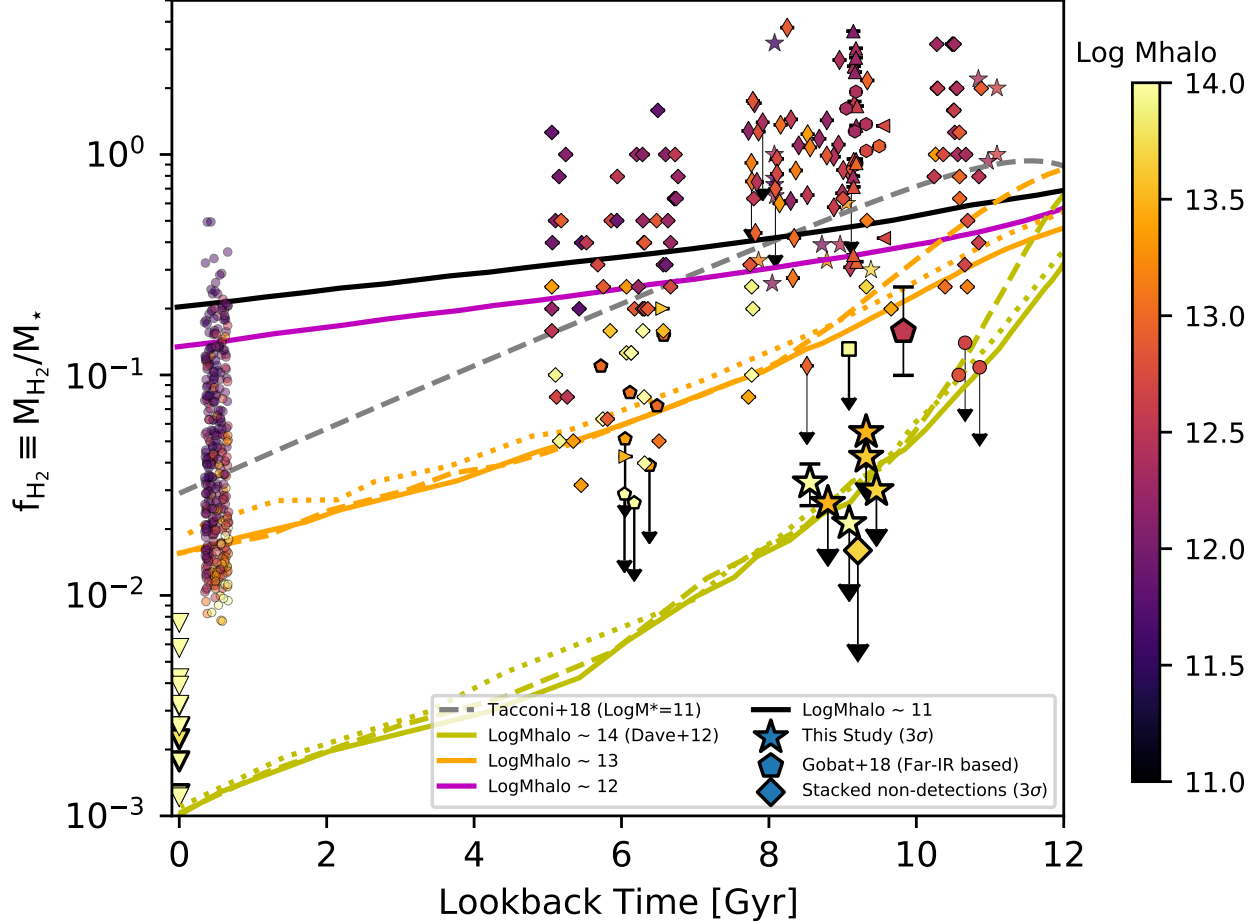


**Figure 6.** Same as Figure 5 but with  $f_{\text{H}_2}(z)$  predictions from analytical equilibrium “bathtub models” that balance gas inflow, outflow, and star-formation. Curves represent halos with masses at  $z=0$  of  $M_{\text{halo}}=10^{11}$  (black),  $10^{12}$  (magenta),  $10^{13}$  (orange) and  $10^{14}$  (yellow)  $M_{\odot}$  published in [Davé et al. \(2012\)](#). Solid lines indicate a model where the mass loading factor for outflowing gas is similar to momentum driven feedback. For halos with final mass  $>10^{13}$  we plot two other feedback prescriptions (dotted and dashed lines, see text) but our conclusions are independent of the stellar feedback prescription. Our data are most consistent with massive halos ( $M_{\text{halo}}=10^{14}M_{\odot}$  at  $z=0$ ) which reached the critical halo mass  $M_{\text{halo}}=10^{12}M_{\odot}$  the earliest, and  $z \sim 4$  (to slow accretion of baryons due to shock heating at the virial radius).

tion by star formation (e.g. [Davé et al. 2012](#); [Finlator & Davé 2008](#); [Bouché et al. 2010](#); [Lilly et al. 2013](#); [Peng & Maiolino 2014](#); [Rathaus & Sternberg 2016](#)). This self-regulation, to first order, appears to describe the behavior of  $f_{\text{H}_2}$  across star forming galaxy populations remarkably well ([Tacconi et al. 2020](#)). However, as halos grow above  $M_{\text{halo}} > 10^{12} M_{\odot}$ , the accretion of baryons is slowed down due to shock heating at the virial radius (e.g. [Dekel & Birnboim 2006](#)). More massive halos reach this critical mass at higher redshifts, spending a longer fraction of cosmic time without accreting new fuel for star formation.

In this section, we compare our observed gas fractions to that predicted using the simple analytic equilibrium model for  $f_{\text{H}_2}(z, M_{\text{halo}})$  outlined in [Davé et al. \(2012\)](#). For a given halo mass and formation redshift,

gas in the galaxy is computed from cosmological accretion as a function of  $M_{\text{halo}}$  ([Dekel et al. 2009](#)), simple stellar and preventative feedback prescriptions that remove gas or keep it hot in the halo, and consumption from the star formation rate. Although the gas fraction in this model is not a self-consistent model for gas evolution because it is computed from the star formation rate with an assumed star formation efficiency, this comparison nonetheless is a simple intuitive tool to qualitatively compare the relative impact of competing processes in galaxies that affect the gas fraction evolution.

In Figure 6 we show a series of these models in comparison to our observations. We show  $f_{\text{H}_2}$  for galaxies in halos that reach masses at  $z=0$  of  $M_{\text{halo}}=10^{11}$  (black),  $10^{12}$  (magenta),  $10^{13}$  (orange) and  $10^{14}$  (yellow)  $M_{\odot}$  published in [Davé et al. \(2012\)](#). Observed galaxies are

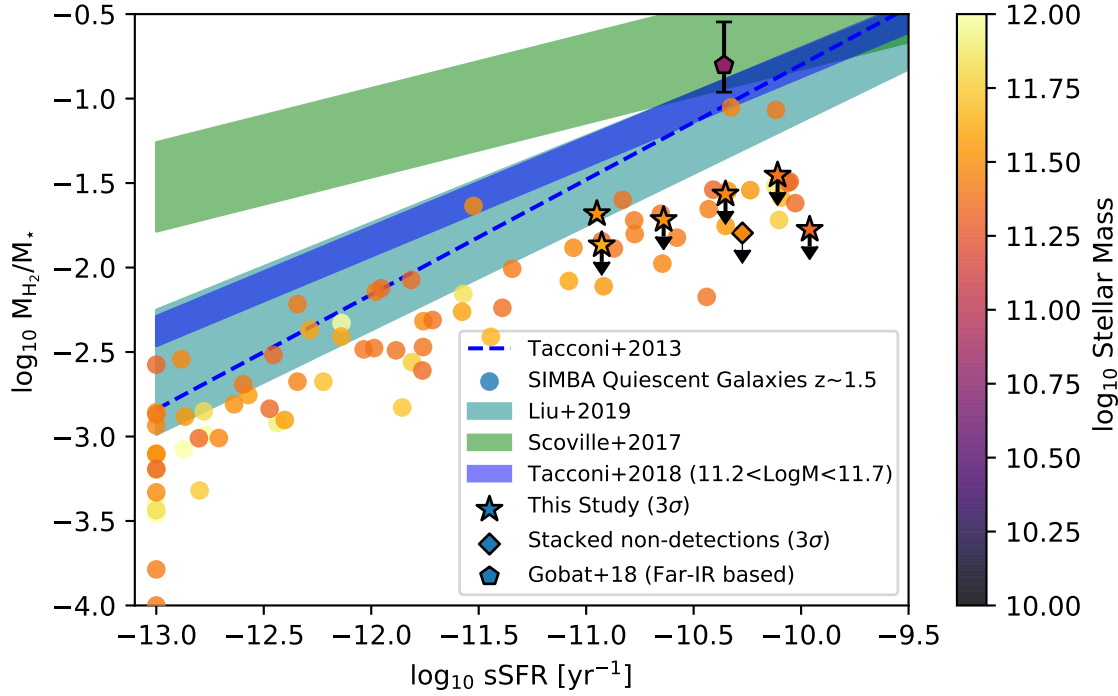


**Figure 7.** Comparison of our observations to extrapolated  $f_{\text{H}_2}$  from scaling relations (Tacconi et al. 2013; Scoville et al. 2017; Tacconi et al. 2018; Liu et al. 2019) as a function of sSFR at fixed  $z = 1.5$ , for  $10.8 < M_* < 11.6$  (indicated by shaded region) to match the range of observations plotted (symbols with black edges; this work and Gobat et al. 2018). SIMBA quiescent galaxies that meet our selection criteria are circles (those with no ongoing SFR have a floor set to  $\log_{10} \text{sSFR} = -13 \text{ yr}^{-1}$ ). Our observed limits are in agreement with the low gas fractions predicted by SIMBA simulations, and both have significantly lower  $f_{\text{H}_2}$  than expected from scaling relations.

color-coded by their inferred halo mass at the redshift of observation, using the stellar mass to halo mass relation of Behroozi et al. 2010 as implemented in HALOTOOLS (Hearin et al. 2017, assuming no scatter, therefore the uncertainties are likely large).

This model predicts that only halos that reach  $10^{14} M_{\odot}$  by  $z = 0$  halt accretion early enough in cosmic time to allow gas consumption to reach the low  $f_{\text{H}_2}$  we observe in our sample. A halo with  $10^{14} M_{\odot}$  at  $z = 0$  reaches this critical halo mass of  $10^{12} M_{\odot}$  at  $z \sim 4$ , and exceeds the quenching threshold (which evolves slightly with  $z$ ) around  $z \sim 3$  (Dekel et al. 2009; Davé et al. 2012). For  $M_{\text{halo}} \lesssim 10^{13} M_{\odot}$  there is not enough time to consume the gas already accreted, and other effects would be required (e.g. gas destruction from feedback) to match our low gas fractions. For  $M_{\text{halo}} > 10^{13}$  we also plot additional mathematical forms to describe the outflow term in the equilibrium model (variations to the stellar feedback prescription, which vary the star formation efficiency). The dotted line indicates a mass loading factor that lowers efficiency at low masses, and the dashed line indicates an additional dependence on metallicity, that decreases gas consumption at low metallicity. These

variations mostly impact growth and gas fraction at low galaxy mass and improve agreement with observations at low masses, but for our case the differences are small and do not impact this result.

Based on these models we speculate that a plausible explanation of our observations is that our galaxies reside in massive halos ( $10^{14} M_{\odot}$  by  $z = 0$ ) that grew above the critical mass of  $10^{12} M_{\odot}$  slowing gas accretion early enough in cosmic time ( $z \sim 4$ ) to reach low gas fractions by  $z \sim 1.5$ . This scenario is qualitatively similar to the idea of cosmological starvation explored in (Feldmann & Mayer 2015).

Estimated halo masses for the ALMA sample are consistent with this picture. The stellar mass to halo mass relation predicts typical  $\log_{10} M_{\text{halo}} / M_{\odot}$  for our sample of 13.5 – 14 at their respective redshifts (Behroozi et al. 2010), in general agreement with inferred halo masses from clustering of quiescent galaxies at  $z > 1$  (e.g. Ji et al. 2018). Furthermore, the relative number density of our ALMA sample from integrating the observed stellar mass function ( $\sim 10^{-5} \text{ Mpc}^{-3}$ ; Tomczak et al. 2014) is similar to that of  $\log_{10} M_{\text{halo}} / M_{\odot} > 13.5$  at our typical redshift  $z \sim 1.4$  (halos that will reach  $10^{14} M_{\odot}$  by

$z=0$ ; calculated using the halo mass function calculator HMF published by Murray et al. 2013, assuming the halo mass function of Behroozi et al. 2013). Were our sample too numerous compared to the requisite mass halos, it would require some fraction of lower mass halos have their gas destroyed more rapidly than implied by the equilibrium model (e.g. via stronger AGN feedback). We note that these ballpark estimates are uncertain owing to scatter in the stellar mass to halo mass relation as well as uncertainties in linking progenitor populations through cumulative number density evolution (Wellons & Torrey 2017; Torrey et al. 2017).

Unfortunately, the simplicity of this analytical model and the significant intrinsic scatter in the stellar mass to halo mass relation precludes a rigorous test of the idea that reaching high halo mass and stopping accretion at early times is the primary driver of low gas fractions. We can only speculate here that this could be a contributing factor. With recent improvements in cosmological simulations, they may provide more realistic and self-consistent comparisons to observables like  $f_{\text{H}_2}$ . We explore these comparisons in the next section.

#### 4.4. Comparison to cosmological simulations

Historically, cosmological simulations have been challenged to match massive galaxies in their abundances over cosmic time, as well as to prevent continued star formation in massive quiescent galaxies (for a review see Somerville & Davé 2015). Recent advances in feedback prescriptions have enabled progress on both of these fronts (Vogelsberger et al. 2014; Schaye et al. 2015; Davé et al. 2019), and now face a new challenge to match the ISM properties such as the cold gas reservoirs we study here (e.g. Narayanan et al. 2012a; Lagos et al. 2014, 2015a,b). Analysis of recent cosmological hydrodynamical simulations indicate that modern implementations of feedback prescriptions for massive galaxies are able to qualitatively reproduce the global scaling relations for star forming galaxies across cosmic time (e.g. Scoville et al. 2017; Tacconi et al. 2018; Liu et al. 2019) as well as the low  $f_{\text{H}_2}$  that are observed in massive and quiescent galaxies by  $z \sim 0$  (e.g. Young et al. 2011; Saintonge et al. 2017; Davis et al. 2016). With our new observations of  $f_{\text{H}_2}$  presented here we can now extend these comparisons to massive quiescent galaxies at  $z \sim 1.5$ . We compare to the predictions for molecular gas reservoirs in the SIMBA simulation (Davé et al. 2019). SIMBA quenches galaxies primarily via its implementation of jet AGN feedback, in which  $\sim 10^4$  km/s jets are ejected bipolarly from low-Eddington ratio black holes. The jets are explicitly decoupled from the ISM, thus presumably the quenching owes to heating and/or removal of halo

gas. SIMBA’s X-ray feedback is important for removing  $\text{H}_2$  from the central regions ( $< 0.5R_e$ ; Appleby et al. 2020), which may also contribute to lowering the global molecular content, in general agreement with evidence for inside out quenching observed in molecular gas reservoirs (Spilker et al. 2019).

We select quiescent galaxies from a snapshot at  $z \sim 1.5$  to match our ALMA target selection criteria:  $\log_{10} M_*/M_\odot > 11.3$  and  $\log_{10} \text{sSFR} < -10 \text{yr}^{-1}$ . The comparison of the  $f_{\text{H}_2}$  in SIMBA galaxies compared to our ALMA observations can be seen in Figure 6. Remarkably, SIMBA predicts low  $f_{\text{H}_2}$  in quiescent galaxies that are consistent with our observational limits. Our ALMA limits on  $f_{\text{H}_2}$  lie at the upper envelope of  $f_{\text{H}_2}$  predicted for SIMBA galaxies of similar mass and sSFR, with the majority of SIMBA galaxies containing  $f_{\text{H}_2} < 3\%$ . 90% of SIMBA galaxies similar to our sample reside in halos with  $\log_{10} M_{\text{halo}}/M_\odot > 13$ , and likely truncated accretion of new gas at earlier times. Better observational constraints on  $t_{\text{dep}}$ , the time evolution of gas reservoirs, and the precision of stellar age diagnostics would be required to link this success directly to the destruction from feedback model, and/or the truncation of new gas accretion as explored in the previous section. SIMBA produces a comparable population of “slow quenchers” and “fast quenchers” (Rodríguez Montero et al. 2019) at these redshifts, and in the future we will examine whether the galaxies consistent with our ALMA limits are preferentially in either category, and measure the associated gas depletion times.

Also in Figure 6 we show the scaling relations based on star forming galaxies across redshifts and quiescent galaxies at  $z \sim 0$  (Scoville et al. 2017; Tacconi et al. 2018; Liu et al. 2019). The shaded regions correspond to the scaling relations at  $z = 1.5$  for  $\log_{10} M_*/M_\odot = 10.8$  (upper bound set by the average mass of the sample studied in Gobat et al. 2018) and  $\log_{10} M_*/M_\odot = 11.6$  (lower bound set by the mass of our most massive galaxy). Both our ALMA limits, as well as the SIMBA predictions, lie well below scaling relations for  $f_{\text{H}_2}(M_*, z, \text{sSFR})$ . This is consistent with the results of Section 4.2, indicating that the simulations also disagree with extrapolations of current scaling relations. Improvements to future scaling relations should include data from surveys such as this one, in the poorly explored parameter space of high redshift and low sSFR.

## 5. CONCLUSIONS

We have conducted the first molecular gas survey of massive quiescent galaxies at  $z > 1$ , using CO(2–1) measured with ALMA. We summarize the findings of our survey as follows:

1. We find very low  $f_{\text{H}_2} < 2\text{--}6\%$  measured for massive quiescent galaxies at  $z \sim 1.5$ . The sample uniformly displays  $f_{\text{H}_2} < 6\%$  and we do not observe any variation with size or stellar density across the large dynamic range of the structural properties within our sample.

2. Depletion times must be rapid as galaxies leave the star forming sequence in order to match our constraints of very low  $f_{\text{H}_2}$ . We estimate an upper limit to the typical depletion time of  $t_{\text{dep}} < 0.6$  Gyr, much shorter than expected from extrapolating current scaling relations to low sSFR.

3. Our low  $f_{\text{H}_2}$  limits are generally consistent with the predictions of an analytical “bathtub” model, for galaxies in massive halos that reach  $\log_{10} M_{\text{halo}}/M_{\odot} = 14$  by  $z=0$ . We speculate that “cosmological starvation” after reaching a critical mass of  $\log_{10} M_{\text{halo}}/M_{\odot} = 12$  ( $z \sim 4$  for these halos), contributed to the rapid decline in  $f_{\text{H}_2}$  required by our observations.

4. Our low  $f_{\text{H}_2}$  limits are consistent with predictions from the recent SIMBA cosmological simulations with realistic AGN feedback, highlighting another success for state-of-the-art models describing the properties of massive quiescent galaxies. This consistency, like the bathtub model, may also point to the simple truncation and consumption picture. However, with our data we cannot rule out that low gas fractions result from gas destruction from feedback or an increase in the efficiency of gas consumption.

Although it may be observationally expensive, concrete tests of current and future galaxy formation models will rely on building larger datasets that probe the molecular gas properties of galaxies with little on-going star formation. Building statistical samples will be challenging and there are a number of approaches that one could take. Real progress will be made with increasing numbers alone. Another possibility would be to combine information about the SFHs with depletion time tracks to follow individual objects back in time. The extraction of these histories from quiescent galaxies at cosmic noon will soon be enabled by the unparalleled capabilities of

the *James Webb Space Telescope (JWST)*. Deep photometric and spectroscopic surveys are planned for Cycle 1 (Williams et al. 2018; Rieke et al. 2019) that will be capable of identifying quiescent galaxies even at  $z > 4$  and reconstructing their star formation histories with unprecedented detail. These will make ideal targets for future ALMA CO surveys to build our understanding of molecular gas in galaxies that have ceased star formation.

This work was performed in part at Aspen Center for Physics, which is supported by National Science Foundation grant PHY-1607611. We acknowledge valuable discussions with Ivo Labbe, Wren Suess, Sandro Tacchella, Sirio Belli. CCW acknowledges support from the National Science Foundation Astronomy and Astrophysics Fellowship grant AST-1701546. JSS is supported by NASA Hubble Fellowship grant #HF2-51446 awarded by the Space Telescope Science Institute, which is operated by the Association of Universities for Research in Astronomy, Inc., for NASA, under contract NAS5-26555. K.E.W. wishes to acknowledge funding from the Alfred P. Sloan Foundation. CAW is supported by the National Science Foundation through the Graduate Research Fellowship Program funded by Grant Award No. DGE-1746060. This paper makes use of the following ALMA data: ADS/JAO.ALMA #2018.1.01739.S, ADS/JAO.ALMA #2015.1.00853.S. ALMA is a partnership of ESO (representing its member states), NSF (USA), and NINS (Japan), together with NRC (Canada), MOST and ASIAA (Taiwan), and KASI (Republic of Korea), in cooperation with the Republic of Chile. The Joint ALMA Observatory is operated by ESO, AUI/NRAO, and NAOJ. The National Radio Astronomy Observatory is a facility of the National Science Foundation operated under cooperative agreement by Associated Universities, Inc. The Cosmic Dawn Center is funded by the Danish National Research Foundation.

## REFERENCES

- Aihara, H., AlSayyad, Y., Ando, M., et al. 2019, PASJ, 71, 114
- Alatalo, K., Lisenfeld, U., Lanz, L., et al. 2016, ApJ, 827, 106
- Appleby, S., Davé, R., Kraljic, K., Anglés-Alcázar, D., & Narayanan, D. 2020, MNRAS, 494, 6053
- Aravena, M., Decarli, R., González-López, J., et al. 2019, ApJ, 882, 136
- Behroozi, P. S., Conroy, C., & Wechsler, R. H. 2010, ApJ, 717, 379
- Behroozi, P. S., Wechsler, R. H., & Conroy, C. 2013, ApJ, 770, 57
- Bell, E. F., van der Wel, A., Papovich, C., et al. 2012, ApJ, 753, 167
- Belli, S., Newman, A. B., & Ellis, R. S. 2014, ApJ, 783, 117
- . 2015, ApJ, 799, 206
- . 2019, ApJ, 874, 17



- Bezanson, R., Spilker, J., Williams, C. C., et al. 2019, *ApJL*, 873, L19
- Bezanson, R., van Dokkum, P., van de Sande, J., Franx, M., & Kriek, M. 2013, *ApJL*, 764, L8
- Birnboim, Y., & Dekel, A. 2003, *MNRAS*, 345, 349
- Bolatto, A. D., Wolfire, M., & Leroy, A. K. 2013, *ARA&A*, 51, 207
- Boselli, A., Cortese, L., Boquien, M., et al. 2014, *A&A*, 564, A66
- Bouché, N., Dekel, A., Genzel, R., et al. 2010, *ApJ*, 718, 1001
- Bruzual, G., & Charlot, S. 2003, *MNRAS*, 344, 1000
- Calette, A. R., Avila-Reese, V., Rodríguez-Puebla, A., Hernández-Toledo, H., & Papastergis, E. 2018, *RMxAA*, 54, 443
- Calzetti, D., Armus, L., Bohlin, R. C., et al. 2000, *ApJ*, 533, 682
- Cassata, P., Giavalisco, M., Williams, C. C., et al. 2013, *ApJ*, 775, 106
- Cecchi, R., Bolzonella, M., Cimatti, A., & Girelli, G. 2019, *ApJL*, 880, L14
- Chabrier, G. 2003, *PASP*, 115, 763
- Choi, E., Ostriker, J. P., Naab, T., et al. 2017, *ApJ*, 844, 31
- Citro, A., Pozzetti, L., Moresco, M., & Cimatti, A. 2016, *A&A*, 592, A19
- Conroy, C., & Gunn, J. E. 2010, *ApJ*, 712, 833
- Conroy, C., Gunn, J. E., & White, M. 2009, *ApJ*, 699, 486
- Croton, D. J., Springel, V., White, S. D. M., et al. 2006, *MNRAS*, 365, 11
- Daddi, E., Bournaud, F., Walter, F., et al. 2010, *ApJ*, 713, 686
- Davé, R., Anglés-Alcázar, D., Narayanan, D., et al. 2019, *MNRAS*, 486, 2827
- Davé, R., Finlator, K., & Oppenheimer, B. D. 2012, *MNRAS*, 421, 98
- Davidzon, I., Ilbert, O., Laigle, C., et al. 2017, *A&A*, 605, A70
- Davis, T. A., Greene, J., Ma, C.-P., et al. 2016, *MNRAS*, 455, 214
- Decarli, R., Walter, F., Aravena, M., et al. 2016, *ApJ*, 833, 70
- Dekel, A., & Birnboim, Y. 2006, *MNRAS*, 368, 2
- Dekel, A., & Burkert, A. 2014, *MNRAS*, 438, 1870
- Dekel, A., Birnboim, Y., Engel, G., et al. 2009, *Nature*, 457, 451
- Di Matteo, T., Springel, V., & Hernquist, L. 2005, *Nature*, 433, 604
- Estrada-Carpenter, V., Papovich, C., Momcheva, I., et al. 2020, *ApJ*, 898, 171
- Feldmann, R., & Mayer, L. 2015, *MNRAS*, 446, 1939
- Feldmann, R., Quataert, E., Hopkins, P. F., Faucher-Giguère, C.-A., & Kereš, D. 2017, *MNRAS*, 470, 1050
- Finlator, K., & Davé, R. 2008, *MNRAS*, 385, 2181
- Forrest, B., Annunziatella, M., Wilson, G., et al. 2020, *ApJL*, 890, L1
- Franx, M., van Dokkum, P. G., Förster Schreiber, N. M., et al. 2008, *ApJ*, 688, 770
- French, K. D., Yang, Y., Zabludoff, A., et al. 2015, *ApJ*, 801, 1
- Freundlich, J., Combes, F., Tacconi, L. J., et al. 2019, *A&A*, 622, A105
- Fumagalli, M., Labbé, I., Patel, S. G., et al. 2014, *ApJ*, 796, 35
- Gaia Collaboration, Brown, A. G. A., Vallenari, A., et al. 2016, *A&A*, 595, A2
- . 2018, *A&A*, 616, A1
- Gensior, J., Kruijssen, J. M. D., & Keller, B. W. 2020, *MNRAS*, 495, 199
- Genzel, R., Tacconi, L. J., Lutz, D., et al. 2015, *ApJ*, 800, 20
- Gobat, R., Daddi, E., Magdis, G., et al. 2018, *Nature Astronomy*, 2, 239
- Gonzaga, S., & et al. 2012, *The DrizzlePac Handbook*
- Grudić, M. Y., Hopkins, P. F., Quataert, E., & Murray, N. 2019, *MNRAS*, 483, 5548
- Hayashi, M., Tadaki, K.-i., Kodama, T., et al. 2018, *ApJ*, 856, 118
- Hayward, C. C., Lanz, L., Ashby, M. L. N., et al. 2014, *MNRAS*, 445, 1598
- Hearin, A. P., Campbell, D., Tollerud, E., et al. 2017, *AJ*, 154, 190
- Hickox, R. C., Wardlow, J. L., Smail, I., et al. 2012, *MNRAS*, 421, 284
- Hodge, J. A., & da Cunha, E. 2020, *arXiv e-prints*, arXiv:2004.00934
- Hopkins, P. F., Hernquist, L., Cox, T. J., et al. 2006, *ApJS*, 163, 1
- Hopkins, P. F., Murray, N., Quataert, E., & Thompson, T. A. 2010, *MNRAS*, 401, L19
- Ji, Z., Giavalisco, M., Williams, C. C., et al. 2018, *ApJ*, 862, 135
- Johnson, B. D., Leja, J. L., Conroy, C., & Speagle, J. S. 2019, *Prospector: Stellar population inference from spectra and SEDs*, , ascl:1905.025
- Kaasinen, M., Scoville, N., Walter, F., et al. 2019, *ApJ*, 880, 15
- Kennicutt, Jr., R. C. 1998, *ApJ*, 498, 541
- Kereš, D., Katz, N., Weinberg, D. H., & Davé, R. 2005, *MNRAS*, 363, 2

- Kriek, M., van Dokkum, P. G., Labbé, I., et al. 2009, *ApJ*, 700, 221
- Lagos, C. d. P., Davis, T. A., Lacey, C. G., et al. 2014, *MNRAS*, 443, 1002
- Lagos, C. d. P., Padilla, N. D., Davis, T. A., et al. 2015a, *MNRAS*, 448, 1271
- Lagos, C. d. P., Crain, R. A., Schaye, J., et al. 2015b, *MNRAS*, 452, 3815
- Lee, B., Giavalisco, M., Whitaker, K., et al. 2018, *ApJ*, 853, 131
- Leitner, S. N., & Kravtsov, A. V. 2011, *ApJ*, 734, 48
- Leja, J., Carnall, A. C., Johnson, B. D., Conroy, C., & Speagle, J. S. 2019a, *ApJ*, 876, 3
- Leja, J., Johnson, B. D., Conroy, C., van Dokkum, P. G., & Byler, N. 2017, *ApJ*, 837, 170
- Leja, J., Johnson, B. D., Conroy, C., et al. 2019b, *ApJ*, 877, 140
- Leroy, A. K., Walter, F., Bigiel, F., et al. 2009, *AJ*, 137, 4670
- Li, Z., French, K. D., Zabludoff, A. I., & Ho, L. C. 2019, *ApJ*, 879, 131
- Lianou, S., Xilouris, E., Madden, S. C., & Barmby, P. 2016, *MNRAS*, 461, 2856
- Lilly, S. J., Carollo, C. M., Pipino, A., Renzini, A., & Peng, Y. 2013, *ApJ*, 772, 119
- Liu, D., Schinnerer, E., Groves, B., et al. 2019, *ApJ*, 887, 235
- Magdis, G. E., Daddi, E., Béthermin, M., et al. 2012, *ApJ*, 760, 6
- Martí-Vidal, I., Vlemmings, W. H. T., Muller, S., & Casey, S. 2014, *A&A*, 563, A136
- Martig, M., Bournaud, F., Teyssier, R., & Dekel, A. 2009, *ApJ*, 707, 250
- Martig, M., Crocker, A. F., Bournaud, F., et al. 2013, *MNRAS*, 432, 1914
- McCracken, H. J., Capak, P., Salvato, M., et al. 2010, *ApJ*, 708, 202
- McDermid, R. M., Alatalo, K., Blitz, L., et al. 2015, *MNRAS*, 448, 3484
- Mowla, L. A., van Dokkum, P., Brammer, G. B., et al. 2019, *ApJ*, 880, 57
- Murray, S. G., Power, C., & Robotham, A. S. G. 2013, *MNRAS*, 434, L61
- Muzzin, A., Marchesini, D., Stefanon, M., et al. 2013a, *ApJS*, 206, 8
- . 2013b, *ApJ*, 777, 18
- Naab, T., & Ostriker, J. P. 2017, *ARA&A*, 55, 59
- Narayanan, D., Bothwell, M., & Davé, R. 2012a, *MNRAS*, 426, 1178
- Narayanan, D., Krumholz, M. R., Ostriker, E. C., & Hernquist, L. 2012b, *MNRAS*, 421, 3127
- Nelson, D., Pillepich, A., Springel, V., et al. 2018, *MNRAS*, 475, 624
- Onodera, M., Renzini, A., Carollo, M., et al. 2012, *ApJ*, 755, 26
- Papovich, C., Labbé, I., Glazebrook, K., et al. 2016, *Nature Astronomy*, 1, 0003
- Peng, C. Y., Ho, L. C., Impey, C. D., & Rix, H.-W. 2002, *AJ*, 124, 266
- Peng, Y.-j., & Maiolino, R. 2014, *MNRAS*, 443, 3643
- Pillepich, A., Springel, V., Nelson, D., et al. 2018, *MNRAS*, 473, 4077
- Privon, G. C., Narayanan, D., & Davé, R. 2018, *ApJ*, 867, 102
- Rathaus, B., & Sternberg, A. 2016, *MNRAS*, 458, 3168
- Renzini, A. 2006, *ARA&A*, 44, 141
- Rieke, M., Arribas, S., Bunker, A., et al. 2019, *BAAS*, 51, 45
- Rodríguez Montero, F., Davé, R., Wild, V., Anglés-Alcázar, D., & Narayanan, D. 2019, *MNRAS*, 490, 2139
- Rowlands, K., Wild, V., Nesvadba, N., et al. 2015, *MNRAS*, 448, 258
- Rudnick, G., Hodge, J., Walter, F., et al. 2017, *ApJ*, 849, 27
- Saintonge, A., Kauffmann, G., Kramer, C., et al. 2011, *MNRAS*, 415, 32
- Saintonge, A., Tacconi, L. J., Fabello, S., et al. 2012, *ApJ*, 758, 73
- Saintonge, A., Catinella, B., Tacconi, L. J., et al. 2017, *ApJS*, 233, 22
- Salim, S., Dickinson, M., Michael Rich, R., et al. 2009, *ApJ*, 700, 161
- Santini, P., Fontana, A., Grazian, A., et al. 2012, *A&A*, 538, A33
- Santini, P., Maiolino, R., Magnelli, B., et al. 2014, *A&A*, 562, A30
- Sargent, M. T., Daddi, E., Bournaud, F., et al. 2015, *ApJL*, 806, L20
- Schaye, J., Crain, R. A., Bower, R. G., et al. 2015, *MNRAS*, 446, 521
- Schreiber, C., Labbé, I., Glazebrook, K., et al. 2018, *A&A*, 611, A22
- Scoville, N., Sheth, K., Aussel, H., et al. 2016, *ApJ*, 820, 83
- Scoville, N., Lee, N., Vanden Bout, P., et al. 2017, *ApJ*, 837, 150
- Silverman, J. D., Daddi, E., Rodighiero, G., et al. 2015, *ApJL*, 812, L23
- Silverman, J. D., Rujopakarn, W., Daddi, E., et al. 2018, *ApJ*, 867, 92

- Simpson, J. M., Smail, I., Wang, W.-H., et al. 2017, *ApJL*, 844, L10
- Skelton, R. E., Whitaker, K. E., Momcheva, I. G., et al. 2014, *ApJS*, 214, 24
- Smercina, A., Smith, J. D. T., Dale, D. A., et al. 2018, *ApJ*, 855, 51
- Smith, M. W. L., Gomez, H. L., Eales, S. A., et al. 2012, *ApJ*, 748, 123
- Somerville, R. S., & Davé, R. 2015, *ARA&A*, 53, 51
- Spilker, J., Bezanson, R., Barišić, I., et al. 2018, *ApJ*, 860, 103
- Spilker, J. S., Bezanson, R., Marrone, D. P., et al. 2016, *ApJ*, 832, 19
- Spilker, J. S., Bezanson, R., Weiner, B. J., Whitaker, K. E., & Williams, C. C. 2019, *ApJ*, 883, 81
- Suess, K. A., Bezanson, R., Spilker, J. S., et al. 2017, *ApJL*, 846, L14
- Tacconi, L. J., Genzel, R., & Sternberg, A. 2020, *arXiv e-prints*, arXiv:2003.06245
- Tacconi, L. J., Neri, R., Genzel, R., et al. 2013, *ApJ*, 768, 74
- Tacconi, L. J., Genzel, R., Saintonge, A., et al. 2018, *ApJ*, 853, 179
- Teimoorinia, H., Bluck, A. F. L., & Ellison, S. L. 2016, *MNRAS*, 457, 2086
- Thomas, D., Maraston, C., Schawinski, K., Sarzi, M., & Silk, J. 2010, *MNRAS*, 404, 1775
- Tomczak, A. R., Quadri, R. F., Tran, K.-V. H., et al. 2014, *ApJ*, 783, 85
- Torrey, P., Wellons, S., Ma, C.-P., Hopkins, P. F., & Vogelsberger, M. 2017, *MNRAS*, 467, 4872
- Utomo, D., Kriek, M., Labbé, I., Conroy, C., & Fumagalli, M. 2014, *ApJL*, 783, L30
- van de Sande, J., Kriek, M., Franx, M., et al. 2013, *ApJ*, 771, 85
- Vogelsberger, M., Genel, S., Springel, V., et al. 2014, *MNRAS*, 444, 1518
- Weinberger, R., Springel, V., Hernquist, L., et al. 2017, *MNRAS*, 465, 3291
- Weinberger, R., Springel, V., Pakmor, R., et al. 2018, *MNRAS*, 479, 4056
- Welch, G. A., Sage, L. J., & Young, L. M. 2010, *ApJ*, 725, 100
- Wellons, S., & Torrey, P. 2017, *MNRAS*, 467, 3887
- Wellons, S., Torrey, P., Ma, C.-P., et al. 2015, *MNRAS*, 449, 361
- Whitaker, K. E., Kriek, M., van Dokkum, P. G., et al. 2012, *ApJ*, 745, 179
- Whitaker, K. E., Pope, A., Cybulski, R., et al. 2017, *ApJ*, 850, 208
- Whitaker, K. E., Labbé, I., van Dokkum, P. G., et al. 2011, *ApJ*, 735, 86
- Whitaker, K. E., Franx, M., Leja, J., et al. 2014, *ApJ*, 795, 104
- Williams, C. C., Giavalisco, M., Porciani, C., et al. 2011, *ApJ*, 733, 92
- Williams, C. C., Giavalisco, M., Cassata, P., et al. 2014, *ApJ*, 780, 1
- Williams, C. C., Giavalisco, M., Lee, B., et al. 2015, *ApJ*, 800, 21
- Williams, C. C., Giavalisco, M., Bezanson, R., et al. 2017, *ApJ*, 838, 94
- Williams, C. C., Curtis-Lake, E., Hainline, K. N., et al. 2018, *ApJS*, 236, 33
- Williams, C. C., Labbe, I., Spilker, J., et al. 2019, *ApJ*, 884, 154
- Wu, P.-F., van der Wel, A., Bezanson, R., et al. 2018, *ApJ*, 868, 37
- Wuyts, S., Labbé, I., Förster Schreiber, N. M., et al. 2008, *ApJ*, 682, 985
- Young, L. M., Bureau, M., Davis, T. A., et al. 2011, *MNRAS*, 414, 940
- Young, L. M., Scott, N., Serra, P., et al. 2014, *MNRAS*, 444, 3408
- Zhang, C., Peng, Y., Ho, L. C., et al. 2019, *ApJL*, 884, L52
- Zolotov, A., Dekel, A., Mandelker, N., et al. 2015, *MNRAS*, 450, 2327